Research Square

Preprints are preliminary reports that have not undergone peer review.
They should not be considered conclusive, used to inform clinical practice,
or referenced by the media as validated information.

Beyond First Order Kinetics: Sensitivity, Identifiability and the Limits of An Extended Quadratic Version for Petroleum Hydrocarbon Bioremediation: Local, Global and Profile-Likelihood Analysis

Yusuf Momoh

loymoly@aol.com

University of Port Harcourt College of Engineering https://orcid.org/0000-0002-7058-9848

Research Article

Keywords: Sensitivity analysis, Sobol indices, Profile likelihood, Parameter identifiability, First-order kinetics, Hindrance, Bioremediation kinetics, Time to 90% removal

Posted Date: November 13th, 2026

DOI: https://doi.org/10.21203/rs.3.rs-10957757/v1

License: This work is licensed under a Creative Commons Attribution 4.0 International License.
Read Full License

Beyond First Order Kinetics: Sensitivity, Identifiability and the Limits of An Extended Quadratic Version for Petroleum Hydrocarbon Bioremediation: Local, Global and Profile-Likelihood Analysis

BY

Yusuf Momoh

Department of Civil Engineering,

University of Port Harcourt College of Engineering, Port Harcourt 500102, Nigeria

Email: loymoly@aol.com

Abstract

A companion study showed that an extended version of the first-order kinetic model, the Hindrance-Modified First-Order Kinetic Model (HM-FOKM), $B(t) = 1 - \exp\left(-Kt + \frac{H}{2}t^2\right)$, outperforms classical first-order kinetics on AICc in 15 of 24 treatments that exhibit genuine quadratic curvature. This study assesses the sensitivity and identifiability of this model through local and global sensitivity analysis, profile-likelihood identifiability analysis, and a new diagnostic: the time to 90 % removal (t_{90}). The local sensitivity functions $S_K$and $S_H$maintain fixed signs throughout the domain ($S_K \geq 0$, $S_H \leq 0$), a simpler structure than that of models whose sensitivities change sign. Because Kand Hare strongly correlated (mean $|\rho| = 0.924$), independent-box Sobol sampling is invalid. A correlation-ratio ensemble reveals that K dominates early ($S_1(K) = 0.98$ at 1 week), while Hovertakes Kat approximately 9.8 weeks Profile-likelihood analysis confirms that Kis better constrained than H. The 95 % confidence interval for Hincludes zero in 10 of 24 treatments (41.7 %), so classical first-order kinetics cannot be excluded even when HM-FOKM is preferred by AICc. The correlation $|\rho(K,H)|$ranges from 0.890 to 0.982, consistent with a general collinearity pattern in two-parameter saturating kinetic models. The t_{90}diagnostic exists only when $K^2 \geq 2H \cdot \ln 10$(equivalently $B_{proj} \geq 0.90$). It was defined for all eleven accelerating treatments and undefined for all thirteen decelerating treatments — a perfect correspondence arising directly from the model's algebra and therefore available as an instantaneous check from the sign of Halone. HM-FOKM's added parameter therefore carries a genuine identifiability cost, yet the model remains structurally simple and can be used with the same confidence as the classical first-order model it extends, provided monitoring programs are designed with these constraints in mind.

Keywords: Sensitivity analysis; Sobol indices; Profile likelihood; Parameter identifiability; First-order kinetics; Hindrance; Bioremediation kinetics; Time to 90 % removal

I. Introduction

Classical first-order kinetics have served as the default model for hydrocarbon biodegradation for decades (Rittmann and McCarty, 2001; Simkins and Alexander, 1984), expressed as $B(t) = 1 - e^{-kt}$,

where k is the first-order rate constant. Its simplicity has made it an entrenched tool for regulators and engineers (Bekins et al., 1998; Chen et al., 2024), but it rests on an assumption rarely met in practice: that the degradation-rate constant remains constant throughout remediation (Alexander, 1999; Boopathy, 2000). Biodegradation is instead a dynamic process shaped by changing microbial communities, shifting substrate composition, and accumulating inhibitory by-products (Leahy and Colwell, 1990; Jiao et al., 2016; Varjani, 2017). Nutrient availability, particularly nitrogen and phosphorus, has been identified as a primary limiting factor controlling the rate and extent of hydrocarbon biodegradation in both marine and soil environments (Atlas & Hazen, 2011). The bioavailability of hydrocarbons, their sorption to soil particles, and the availability of essential nutrients are all critical factors limiting the rate of biodegradation (Megharaj et al., 2011).

The most critical limitation of first-order kinetics is their inability to detect or quantify deceleration in degradation trajectories. When a trajectory decelerates, first-order kinetics systematically overestimate late-stage degradation, with practical consequences for regulatory compliance and remediation-cost estimation (Chen et al., 2024; Ossai et al., 2020; Ambaye et al., 2022). Existing alternatives have limitations of their own: the Modified Gompertz model requires three empirical parameters with no direct biological correspondence (Zwietering et al., 1990; Jakubauskaite et al., 2024), while the Grau second-order model assumes constant microbial biomass, inconsistent with adaptive field communities (Grau et al., 1975; Nweke and Nwabanne, 2021).

A companion study introduced the Hindrance-Modified First-Order Kinetic Model (HM-FOKM) as a minimal, two-parameter extension capable of detecting and quantifying deceleration. Validated across five independent datasets spanning twenty-four treatments — a primary eight-week field trial (Momoh, 2025) and four external datasets spanning Nigeria, Iran, Australia and Spain (Ahmadi et al., 2016; Udume, Abu and Momoh, 2023; Dike et al., 2024; Ritoré et al., 2025) — HM-FOKM achieved a favourable AICc in fifteen treatments (62.5 %), with its advantage tracking curvature strength rather than sample size.

The model expresses biodegradability as $B(t) = 1 - \exp\left(-Kt + \frac{H}{2}t^2\right)$, where $K$is the initial rate constant and $H$the hindrance coefficient; $H > 0$indicates deceleration, $H < 0$acceleration, and $H = 0$recovers first-order kinetics exactly. That study also introduced two diagnostics from the fitted parameters — the transition time $t_{trans} = K/H$and the projected ultimate biodegradability B_{proj}— and reported profile-likelihood confidence intervals for a subset of treatments, showing that H, while informative, is not always tightly constrained.

What that study did not provide is a systematic characterisation of how sensitive the model's output is to each parameter, nor a rule for predicting when $H$is likely to be well identified before fitting. Local

sensitivity analysis is analytically tractable but describes only infinitesimal perturbations at a point (Saltelli et al., 2008; Hamby, 1994). Global sensitivity analysis instead apportions output variance across the full parameter space, separating each parameter's independent contribution from its interaction with others (Sobol, 2001; Saltelli et al., 2010) — a distinction local method cannot make (Borgonovo and Plischke, 2016). Profile-likelihood analysis provides a third perspective, quantifying parameter uncertainty directly from data while correctly capturing asymmetry in the likelihood surface, unlike asymptotic intervals (Venzon and Moolgavkar, 1988; Bates and Watts, 1988; Raue et al., 2009).

This study applies all three approaches to HM-FOKM, extends the partial profile-likelihood treatment given previously to all 24 treatments, and introduces one further diagnostic: the time to 90 % removal, t_{90}, a widely used regulatory benchmark (Zwietering et al., 1990; USEPA, 1996) whose existence condition, as shown below, coincides exactly with a threshold on B_{proj}already implicit in the validation study's findings. Specifically, this study addresses four questions:

a. How do the local sensitivities to K and H behave across time, and do they change sign as some related models' sensitivities do?

b. Which parameter dominates the model's output at different monitoring horizons, and how large is their interaction?

c. What does full profile-likelihood analysis of all 24 treatments reveal about the practical identifiability of Kand H?

d. Does t_{90} add genuine, non-redundant value to the existing t_{trans}/B_{proj}toolkit?

2. Materials and Methods

2.1 Model Derivation

2.1.1 Why Classical First-Order Kinetics Fails in Tilled /Mixed Soil or Field Systems

Classical first-order kinetics assumes the degradation rate constant kis fixed for the entire remediation period:

$$\frac{dB}{dt} = k(1 - B),\ B(t) = 1 - e^{-kt}. \qquad (1)$$

This is a strong and, in field-scale tilled soil systems, frequently false assumption. Two competing processes act on the microbial community's effective catalytic capacity throughout remediation, and neither is captured by a fixed k.

Inhibitor accumulation. As biodegradation proceeds, partially oxidized intermediates and other inhibitory metabolic by-products accumulate in the soil matrix. These by-products suppress microbial activity, progressively lowering the effective rate constant — the mechanistic basis of "hindrance."

Tilling-driven volatilization. Regular tilling, standard practice in field-scale open-soil bioremediation, mechanically turns the soil, enhancing oxygen transfer and volatilizing a portion of the accumulated inhibitory by-products. Critically, because tilling is a scheduled mechanical intervention rather than a concentration-driven chemical process,

its removal action is well-approximated as constant per unit time — i.e., zero-order — under a regular tilling schedule, regardless of how much inhibitor happens to be present at that moment.

The net balance of these two processes — accumulation versus tilling-driven removal — determines whether the system's catalytic capacity degrades, improves or holds steady over time. This is the physical origin of the Hindrance Index; it is not an arbitrary mathematical add-on to first-order kinetics, but the minimal extension that lets these two competing, field-relevant processes be represented explicitly.

2.1.2 Inhibitor Mass Balance

Let $I(t)$ denote the effective level of inhibitory by-products present in the soil at time t. Over the early-to-mid remediation window that this model is intended for — typically the first several weeks to months of a field trial, before the readily degradable fraction is substantially exhausted — two simplifying observations hold.

First, the production rate of inhibitory by-products, p, is approximately constant. This follows because ongoing degradation activity, which generates these by-products as a consequence of its own catalytic turnover, is itself changing only slowly relative to the monitoring window under consideration — the readily degradable fraction has not yet been substantially depleted, so the flux of new intermediates being generated per unit time does not itself vary sharply.

Second, the tilling-driven volatilization removal rate, v, is approximately constant — zero-order — because it is set by the mechanical tilling schedule (frequency, depth, soil turnover per pass) rather than by the instantaneous inhibitor concentration.

Under these two approximations, the inhibitor mass balance is

$$\frac{dI}{dt} = p - v. \qquad (2)$$

Since the right-hand side is constant, this integrates immediately from the initial condition $I(0) = I_0$:

$$I(t) = I_0 + (p - v)t. \qquad (3)$$

This is the critical step in the derivation: the linear-in-time growth (or decay) of the inhibitor level is a direct, unforced consequence of the zero-order tilling-removal assumption — it is derived here, not assumed. If tilling-driven volatilization were instead concentration-dependent (first-order in I, for instance), Equation (3) would be exponential rather than linear, and the resulting kinetic model would not reduce to the simple quadratic-exponent form developed below. The tilling-based zero-order assumption is therefore the specific physical commitment that makes HM-FOKM's closed-form tractability possible.

2.1.3 The Rate Constant as a Function of Accumulated Inhibitor

The degradation rate constant is suppressed in direct proportion to the level of inhibitor present, reflecting the standard assumption that inhibitory metabolites act on the microbial community's catalytic machinery in a dose-dependent manner over the range of concentrations relevant to this model:

$$k(t) = k_0 - \alpha \cdot I(t), \qquad (4)$$

where k_0 is the intrinsic, uninhibited rate constant the community would express in the complete absence of accumulated by-products, and $\alpha > 0$ is the inhibition sensitivity — how strongly a given level of inhibitor suppresses catalytic activity for this particular microbial community and contaminant system. Substituting Equation (3):

$$k(t) = k_0 - \alpha I_0 - \alpha(p - v)t. \qquad (5)$$

2.1.4 Collapsing to the Lumped, Fittable Parameters K and H

Equation (5) contains four underlying mechanistic quantities (k_0, α, I_0, and the difference $p - v$), but only two independent combinations of them actually appear, and these are exactly what can be identified from a biodegradability time series. Define:

$$K \equiv k_0 - \alpha I_0, \qquad (6)$$

$$H \equiv \alpha(p - v). \qquad (7)$$

Substituting into Equation (5):

$$k(t) = K - Ht. \qquad (8)$$

K(week^{-1})) is the initial rate constant — the intrinsic rate k_0, discounted by whatever inhibitor level I_0 is already present at the start of monitoring ($t = 0$). It is not, in general, identical to the intrinsic k_0, but the two coincide when $I_0 = 0$ (no pre-existing inhibitor burden at the start of the trial).

H(week^{-2}) is the hindrance coefficient — the inhibition sensitivity α multiplied by the net rate of inhibitor accumulation, $p - v$. It is a signed quantity by construction: its sign is determined entirely by whether by-product production outpaces tilling-driven removal, or vice versa.

2.1.5 Physical Interpretation of the Sign of H

The physical interpretation of the hindrance coefficient H follows directly from its definition $H = \alpha(p - v)$. Because the inhibition sensitivity α is strictly positive, the sign of H is determined entirely by the balance between by-product production and tilling-driven removal.

I. **Accelerating regime ($H < 0; v > p$)**

When tilling removes by-products faster than they form ($v > p$), the hindrance coefficient is negative ($H < 0$). Under these conditions, the system exhibits accelerating behaviour: the rate constant increases over time as tilling keeps the system progressively cleaner than its production rate would allow. This regime corresponds to a situation where mechanical intervention is more than sufficient to offset the ongoing generation of inhibitory metabolic by-products, leading to progressively less inhibition over time.

II. **Classical first-order regime ($H = 0; v = p$)**

When production and removal exactly balance ($p = v$), the hindrance coefficient is zero ($H = 0$). Under these conditions, classical first-order kinetics are recovered exactly: the rate constant is genuinely constant because tilling exactly offsets ongoing by-product generation. This is not merely a mathematical convenience but a specific, testable

physical condition: the tilling schedule in use is exactly sufficient to offset the contaminant system's own by-product generation rate.

III. Decelerating regime ($H > 0; p > v$)

When production outpaces tilling's removal capacity ($p > v$), the hindrance coefficient is positive ($H > 0$). Under these conditions, the system exhibits decelerating behaviour: the rate constant decreases over time as inhibitor accumulates faster than tilling can clear it. This is the regime of greatest practical concern, as it corresponds to a situation where the system's degradation capacity is progressively compromised, and intervention may be required to prevent a genuine stall before the remediation target is achieved.

This is the physically substantive content of the model: $H = 0$ is not merely "no hindrance term" in a mathematical sense, but corresponds to the specific, testable field condition that the tilling schedule in use is exactly sufficient to offset the contaminant system's own by-product generation rate. A fitted H significantly different from zero is therefore direct evidence, from the biodegradability trajectory alone, that the tilling regime is either more than adequate ($H < 0$) or insufficient ($H > 0$) for that particular soil/contaminant/amendment combination.

This interpretation provides a direct link between the model's fitted parameters and actionable management decisions:

- If H is significantly positive, the tilling regime should be intensified or supplemented with additional interventions (e.g., increased tilling frequency, depth, or aeration; addition of amendments that enhance volatilization or sorption of inhibitors).
- If H is significantly negative, the current regime is more than adequate, and management effort could potentially be reduced without compromising degradation performance (e.g., fewer tilling passes, reduced energy input, or reallocation of labour to other constraints).

In this way, the sign and magnitude of H function as a diagnostic index of the adequacy of the tilling strategy relative to the intrinsic by-product generation dynamics of the system.

2.1.6 Integration to Obtain the Biodegradability Trajectory $\mathrm{B(t)}$

Substituting the linear rate constant $\mathrm{k(t) = K - Ht}$(Equation 8) into the governing biodegradation equation:

$$\frac{\mathrm{dB}}{\mathrm{dt}} = \mathrm{k(t)(1 - B) = (K - Ht)(1 - B).} \qquad (9)$$

Separate variables:

$$\frac{\mathrm{dB}}{\mathrm{1 - B}} = \mathrm{(K - Ht)\,dt.} \qquad (10)$$

Integrate both sides from $\mathrm{t = 0}$($\mathrm{B = 0}$, the start of monitoring, by definition of Bas fractional removal) to t($\mathrm{B = B(t)}$):

$$\int_0^{B(t)} \frac{dB'}{1-B'} = \int_0^t (K - H\tau)\, d\tau. \qquad (11)$$

The left-hand side integrates to $-\ln(1-B(t))$(using $-\ln(1-0) = 0$ at the lower limit); the right-hand side integrates to $Kt - (H/2)t^2$:

$$-\ln(1-B(t)) = Kt - \frac{H}{2}t^2. \qquad (12)$$

Exponentiating and rearranging:

$$B(t) = 1 - \exp\left(-Kt + \frac{H}{2}t^2\right). \qquad (13)$$

This is the HM-FOKM operative equation. Setting $H = 0$ in Equation (13) recovers classical first-order kinetics identically — not as an asymptotic approximation, since the entire $(H/2)t^2$term vanishes exactly, correspond ing physically to the exact tilling/production balance case identified in Section 2.1.5.

2.1.7 The Instantaneous Hazard Function and the Model's Valid Domain

The rate constant at time t, $k(t)$from Equation (8), plays the role of an instantaneous hazard function — the rate of degradation at time t, conditional on the system having reached time $t$without having already exhausted its capacity to degrade:

$$h(t) = K - Ht. \qquad (14)$$

This quantity is physically meaningful only while $h(t) \geq 0$: a negative hazard would imply the system actively re-contaminating itself, which the underlying inhibitor/tilling mass balance (Section 2.1.2) does not support once the inhibitor level has already fully suppressed catalytic activity. For $H > 0$, non-negativity of $h(t)$restricts the model's valid domain to

$$t \leq t_{trans} = \frac{K}{H}. \qquad (15)$$

For $H \leq 0$, $h(t)$never reaches zero for any $t > 0$(it either stays constant at K, or grows without bound as tilling continuously outpaces production), so no such restriction applies and the model is valid for all $t \geq 0$.

2.1.8 Diagnostic Metric I — Transition Time (t_{trans})

Directly from Equation (15):

$$t_{trans} = \frac{K}{H} \text{ (defined only for } H > 0). \qquad (16)$$

Physically, $t_{trans}$is the projected time at which continued current conditions — the same tilling schedule, the same net by-product-production rate — would drive the rate constant to zero, meaning the modelled degradation process would theoretically cease. It is a projection under the assumption of unchanged field practice, not a prediction that

degradation will literally stop; in practice it signals the point by which intervention (increased tilling frequency, nutrient replenishment, aeration) would be needed to prevent a genuine stall.

2.1.9 Diagnostic Metric 2 — Projected Ultimate Biodegradability (B_{proj})

Evaluating the operative equation (13) at $t = t_{trans} = K/H$:

$$B_{proj} = B(t_{trans}) = 1 - \exp\left(-K \cdot \frac{K}{H} + \frac{H}{2} \cdot \left(\frac{K}{H}\right)^2\right). \qquad (17)$$

Simplify the exponent:

$$-\frac{K^2}{H} + \frac{K^2}{2H} = -\frac{K^2}{2H}, \qquad (18)$$

giving

$$B_{proj} = 1 - \exp\left(-\frac{K^2}{2H}\right). \qquad (19)$$

B_{proj}represents the maximum fraction of contaminant degraded before the rate constant reaches zero under the projected trajectory — a direct, field-relevant estimate of the remediation ceiling achievable without a change in tilling or amendment strategy, for any decelerating ($H > 0$) treatment.

2.1.10 Diagnostic Metric 3 — Time to 90 % Removal (t_{90})

Setting $B(t) = 0.90$in Equation (13):

$$1 - \exp\left(-Kt + \frac{H}{2}t^2\right) = 0.90, \qquad (20)$$

$$\exp\left(-Kt + \frac{H}{2}t^2\right) = 0.10. \qquad (21)$$

Taking the natural logarithm:

$$-Kt + \frac{H}{2}t^2 = \ln(0.10) = -\ln(10). \qquad (22)$$

Rearranging into standard quadratic form in t, with $a = H/2$, $b = -K$, $c = \ln(10)$:

$$\frac{H}{2}t^2 - Kt + \ln(10) = 0. \qquad (23)$$

Applying the quadratic formula:

$$t = \frac{K \pm \sqrt{K^2 - 2H \cdot \ln(10)}}{H}. \qquad (24)$$

The two roots correspond to the two times at which the (non-monotonic, for $H > 0$) exponent would cross the required threshold if followed indefinitely. The physically relevant root is the smaller one — the first genuine crossing, occurring before the trajectory turns over at t_{trans}:

$$t_{90} = \frac{K - \sqrt{K^2 - 2H \cdot \ln(10)}}{H}. \qquad (25)$$

2.1.10.1 Existence Condition

The time to 90 % removal, t_{90}, is real-valued only when the expression under the square root in Equation (25) is non-negative. This requirement gives the existence condition:

$$K^2 - 2H \cdot \ln(10) \geq 0 \;\Leftrightarrow\; H \leq \frac{K^2}{2\ln(10)}. \qquad (26)$$

This condition has a straightforward physical interpretation that depends on the sign of H. When $H \leq 0$, the condition is automatically satisfied because the right-hand side of the inequality is always positive (for $K \neq 0$). This means that accelerating systems ($H < 0$) and classical first-order systems ($H = 0$) will always eventually reach 90 % removal—the degradation rate either increases over time or remains constant, so there is no fundamental barrier to reaching the 90 % threshold.

When $H > 0$, however, the condition is satisfied only when hindrance is weak relative to the square of the initial rate constant. Physically, this corresponds to a situation where tilling-driven removal falls short of by-product production, but by a small enough margin that 90 % removal remains achievable before the projected stall at t_{trans}. If $H$is too large—meaning inhibitor accumulation outpaces tilling removal too severely—the system will stall before reaching 90 % removal, and t_{90}will be undefined. The boundary case $H = K^2/(2\ln 10)$corresponds to the situation where the system reaches exactly 90 % removal at the precise moment the hazard function reaches zero at t_{trans}.

2.1.10.2 Exact Equivalence to $B_{proj} \geq 0.90$

The existence condition for t_{90} is algebraically identical to requiring $B_{proj} \geq 0.90$. Starting from the definition of B_{proj} in Equation (19), requiring $B_{proj} \geq 0.90$ gives:

$$\exp\left(-\frac{K^2}{2H}\right) \leq 0.10 \;\Rightarrow\; -\frac{K^2}{2H} \leq -\ln(10) \;\Rightarrow\; \frac{K^2}{2H} \geq \ln(10). \qquad (27)$$

For $H > 0$, multiplying through by $2H$(which is positive, so the inequality direction is preserved) yields:

$$K^2 \geq 2H \cdot \ln(10). \qquad (28)$$

This is identical to the existence condition in Equation (26). Therefore, t_{90}exists if and only if $B_{\mathrm{proj}} \geq 0.90$. This equivalence is a free corollary of any already-computed B_{proj}, requiring no separate calculation to check. For practitioners, this means that a single check of B_{proj}against the 0.90 threshold suffices to determine whether t_{90}exists—there is no need to compute t_{90}separately for this purpose.

2.1.10.3 Reduction to the Classical First-Order Expression as $H \to 0$

As Happroaches zero, the HM-FOKM expression for t_{90}must reduce to the familiar classical first-order expression $t_{90} = \ln(10)/K$. To verify this, write $a = 2H \cdot \ln(10)$and expand the square root in Equation (25) via a first-order Taylor series, valid for small H:

$$\sqrt{K^2 - a} \approx K\sqrt{1 - \frac{a}{K^2}} \approx K\left(1 - \frac{a}{2K^2}\right) = K - \frac{a}{2K} = K - \frac{H \cdot \ln(10)}{K}. \qquad (29)$$

Substituting this approximation into Equation (25):

$$t_{90} \approx \frac{K - (K - H \cdot \ln(10)/K)}{H} = \frac{H \cdot \ln(10)/K}{H} = \frac{\ln(10)}{K}, \qquad (30)$$

which is exactly the classical first-order expression. This reduction was verified both analytically via the Taylor-series argument above and numerically: direct evaluation of Equation (25) at $H = 10^{-6}$agreed with $\ln(10)/K$to within 10^{-4}weeks across the full empirical range of Kobserved in the validation dataset (0.0111 to 0.4873 week $^{-1}$). This confirms that HM-FOKM is a strict generalisation of classical first-order kinetics, recovering the standard result exactly in the limit of vanishing hindrance.

2.2 Data Sources

Five independent datasets were compiled for validation, spanning twenty-four treatments in total. The datasets differ substantially in scale, duration, contaminant type, amendment class and geography, providing a rigorous test of the model's generalizability.

2.2.1 Dataset 1: Primary Field Trial (Momoh, 2025)

The primary dataset comprised seven treatments from a field trial of crude oil–contaminated tropical agricultural soil at the University of Port Harcourt, Nigeria. Treatments included an unamended control, calcined bone char (CBC) at three dose levels (2,200, 8,900 and 15,600 kg ha^{-1}), and NPK fertilizer at three dose levels (2,200, 8,900 and 15,600 kg ha^{-1}). Monitoring was conducted over eight weeks at weekly intervals (n = 8) with three replicates per treatment. Total hydrocarbon content was determined gravimetrically following extraction with dichloromethane. Biodegradability was calculated as $B(t) = (C_0 - C_t)/C_0$, where C_0 is the initial total hydrocarbon content and C_t is the remaining hydrocarbon content at time t. This dataset represents the author's original, numerically recorded data, requiring no digitization.

2.2.2 Dataset 2: Co-Composting of Oil-Based Drill Cuttings (Ahmadi et al., 2016)

The first external validation dataset included four pilots from co-composting of oil-based drill cuttings (initial total petroleum hydrocarbon concentration = 360.46 g kg^{-1}) amended with cow manure at four mixing ratios: Pilot A (0:1 control), Pilot B (5.6:1 manure-to-cutting ratio), Pilot C (10:1 manure-to-cutting ratio) and Pilot D (20:1 manure-to-cutting ratio). Total petroleum hydrocarbon (TPH) was monitored over 60 days at 15-day intervals (n = 5) via gas chromatography with flame ionization detection (GC-FID) following ultrasonic extraction with dichloromethane. This dataset was published with full numerical tables and used directly without digitization. Biodegradability was calculated as $B(t) = (TPH_0 - TPH_t)/TPH_0$.

2.2.3 Dataset 3: Water Hyacinth and Spent Mushroom Compost Amendment (Udume, Abu and Momoh, 2023)

The second external dataset comprised six treatments from crude oil–contaminated soil amended with NPK fertilizer, water hyacinth (WH), spent mushroom compost (SMC), combinations thereof (SMC+WH), sterilized soil with WH, and an unamended control. **Monitoring was conducted over 8 weeks at four time points (n = 4).** Biodegradability was reported as percentage degradation of total petroleum hydrocarbon, determined gravimetrically following Soxhlet extraction with hexane. This dataset was available only as published figures, requiring digitization. Digitization was performed using pixel-coordinate calibration implemented in Python (NumPy/SciPy) with the following steps: image import and axis calibration against internal gridlines, curve isolation by RGB colour thresholding, and marker centroid extraction at each sampling day. Digitized endpoints were validated against reported values in the source article, with agreement ranging from 0.2% to 2.4%. The digitization uncertainty was estimated at approximately ±1–3 percentage points in B(t) at intermediate times.

2.2.4 Dataset 4: Biochar-Assisted Bioremediation (Dike et al., 2024)

The third external dataset included three treatments from petroleum hydrocarbon–contaminated soil: biochar amendment (B), biochar with sodium azide (NaN_3) partial inhibition (BN), and unamended control (C). **Monitoring was conducted over 24 weeks (168 days) at irregular intervals (n = 6).** Total petroleum hydrocarbon was determined by GC-FID following solvent extraction. Biodegradability was calculated as percentage removal relative to initial concentration. This dataset was available only as published figures, requiring digitization using the same procedure described in Section 2.2.3. Digitized endpoints were validated against reported differences (<25 mg kg^{-1}) in the source article.

2.2.5 Dataset 5: Industrial Liquid By-Product Amendment (Ritoré et al., 2025)

The fourth external dataset comprised four treatments from crude oil–contaminated soil amended with industrial liquid by-products: NA (control), SD, LY and SC. **Monitoring was conducted over 20 weeks (140 days) (n = 7).** Total petroleum hydrocarbon was determined by GC-FID following extraction with acetone/hexane. Biodegradability was calculated as percentage removal relative to initial concentration. This dataset was available only as published figures, requiring digitization using the same procedure described in Section 2.2.3. Digitized endpoints were validated exactly (0.0% error) against reported values in the source article. An internal-consistency check was also performed: half-life values reported in the source article reproduced the first-order rate constant k to within 0.4 days, confirming the reliability of the digitization.

2.3 Model Fitting Procedure

2.3.1 Fitting Algorithm

The HM-FOKM (Equation 13) and classical first-order model ($B(t) = 1-e^{-kt}$) were each fitted independently to every treatment–dataset time series using nonlinear least-squares regression (Motulsky and Ransnas, 1987; Bates and Watts, 1988). For datasets reported in days (Datasets 2–5), time was converted to weeks (t = days/7) to retain consistency with week^{-1} units.

A two-stage optimization strategy was employed to reduce the risk of convergence to local minima — particularly important given the small sample sizes (n = 3–8 time points per series). The first stage consisted of a global differential-evolution search (Storn and Price, 1997) across physiologically plausible parameter ranges: $K \in [0.001, 2.0]$ week^{-1}, $H \in [-1.0, 1.0]$ week^{-2}, and $k \in [0.001, 2.0]$ week^{-1}. The second stage consisted of local Levenberg–Marquardt refinement (Marquardt, 1963) starting from the global optimum identified in the first stage.

Convergence was confirmed by inspecting the final gradient norm (ensuring it fell below 10^{-6}) and parameter stability across multiple starting points. For each treatment, the fitting procedure was repeated from three independent starting parameter sets to verify that the global optimum had been identified.

2.3 Model Fitting Procedure

2.3.1 Fitting Algorithm

The HM-FOKM (Equation 13) and classical first-order model $\left(B(t) = 1 - e^{-kt}\right)$were each fitted independently to every treatment–dataset time series using nonlinear least-squares regression (Motulsky and Ransnas, 1987; Bates and Watts, 1988). For datasets reported in days (Datasets 2–5), time was converted to weeks ($t = \text{days}/7$) to retain consistency with week $^{-1}$ units.

A two-stage optimization strategy was employed to reduce the risk of convergence to local minima — particularly important given the small sample sizes ($n = 3$–8 time points per series). The first stage consisted of a global differential-evolution search (Storn and Price, 1997; Price et al., 2005) across physiologically plausible parameter ranges: $K \in [0.001, 2.0]$week $^{-1}$, $H \in [-, 1.01.0]$week $^{-2}$, and $k \in [0.001, 2.0]$week $^{-1}$. The second stage consisted of local Levenberg–Marquardt refinement (Marquardt, 1963; More, 1978) starting from the global optimum identified in the first stage.

Convergence was confirmed by inspecting the final gradient norm (ensuring it fell below 10^{-6}) and parameter stability across multiple starting points. For each treatment, the fitting procedure was repeated from three independent starting parameter sets to verify that the global optimum had been identified.

2.3.2 Goodness-of-Fit Metrics

For each treatment–dataset combination and for both models, four fit metrics were computed. The coefficient of determination

$$R^2 = 1 - \frac{\sum (B_{\text{obs}} - B_{\text{pred}})^2}{\sum (B_{\text{obs}} - \bar{B}_{\text{obs}})^2} \qquad (31)$$

quantifies the fraction of variance explained by the model. The root mean square error

$$\mathrm{RMSE} = \sqrt{\frac{1}{n}\sum\left(B_{\mathrm{obs}} - B_{\mathrm{pred}}\right)^2} \qquad (32)$$

gives the absolute prediction error in the units of $B(t)$. The Akaike Information Criterion

$$\mathrm{AIC} = n\ln\left(\frac{\mathrm{SSE}}{n}\right) + 2p \qquad (33)$$

and the corrected Akaike Information Criterion

$$\mathrm{AICc} = \mathrm{AIC} + \frac{2p(p+1)}{n-p-1} \qquad (34)$$

penalize model complexity relative to sample size, where $\mathrm{SSE} = \sum\left(B_{\mathrm{obs}} - B_{\mathrm{pred}}\right)^2$, $p$is the number of fitted parameters ($p = 1$ for classical first-order; $p = 2$for HM-FOKM), and $n$is the number of observations. Lower AICc indicates greater parsimony; a difference $\Delta\mathrm{AICc} \geq 2$is considered meaningful evidence and $\Delta\mathrm{AICc} \geq 6$strong evidence favouring the model with the lower AICc (Burnham and Anderson, 2002).

2.4 Local Sensitivity Analysis

The local sensitivity functions were obtained by direct partial differentiation of $B(t)$with respect to each parameter. Write $f(t) = -Kt + (H/2)t^2$, so that $B(t) = 1 - e^{f(t)}$, and let $g(t) \equiv e^{f(t)} = 1 - B(t)$. The local sensitivities are obtained by direct partial differentiation using the chain rule.

For K:

$$S_K(t) = \frac{\partial B}{\partial K} = -g(t)\cdot\frac{\partial f}{\partial K} = -g(t)\cdot(-t) = t\cdot g(t) = t[1 - B(t)]. \qquad (35)$$

For H:

$$S_H(t) = \frac{\partial B}{\partial H} = -g(t)\cdot\frac{\partial f}{\partial H} = -g(t)\cdot\frac{t^2}{2} = -\frac{t^2}{2}[1 - B(t)]. \qquad (36)$$

Both expressions were verified against central finite-difference approximations of $B(t)$(step size 10^{-5}–10^{-6}) across a grid of (K, H, t)combinations spanning the empirical parameter range; agreement was within numerical precision throughout the model's physically valid domain ($t < t_{\mathrm{trans}}$ when $H > 0$). For $H > 0$both functions are reported only up to t_{trans}, since $B(t)$— and consequently its derivatives — lose physical meaning once the hazard function crosses zero and the fitted trajectory would imply reversal of degradation.

Since $0 \leq B(t) \leq 1$throughout the model's physically valid domain, $1 - B(t) \geq 0$always. Consequently, $S_K(t) \geq 0$for all $t \geq 0$(equality only at $t = 0$), and $S_H(t) \leq 0$for all $t \geq 0$. Both sensitivities therefore have fixed sign throughout the model's valid domain — there is no time point at which increasing Kdecreases $B(t)$, nor any time point at which increasing Hincreases $B(t)$. This fixed-sign behaviour is not merely a mathematical curiosity: it reflects the physical construction of $K$and Hdirectly. $K$is, by Equation (6), a catalytic capacity parameter — increasing it can only ever increase the rate at which degradation proceeds. $H$is, by Equation (7), a net hindrance parameter — increasing it (more production relative to tilling-removal) can only ever suppress degradation. Both sensitivities are zero at $t = 0$, since no time has yet elapsed for either the initial rate advantage or the accumulating/dissipating hindrance to manifest, and both grow in magnitude with time as their respective mechanisms compound. This monotonicity is a desirable property for parameter interpretation, as it ensures that the effect of each parameter on the model output is unambiguous (Hamby, 1994; Saltelli et al., 2008).

2.5 Global Sensitivity Analysis

Two global sensitivity analyses were performed using methods appropriate to each output's structure.

2.5.1 $B(t)$at Fixed Monitoring Times: Correlation-Ratio Analysis

Standard variance-based Sobol analysis (Sobol, 2001; Saltelli et al., 2010), which requires independent sampling of inputs across their marginal ranges, is not valid for $B(t)$evaluated at a fixed external monitoring time for two reasons. First, $K$and $H$are strongly correlated in the fitted data (mean $|\ \rho\ | = 0.924$; see Section 3.6), and independent sampling violates this correlation structure. Second, HM-FOKM is mathematically unbounded for $H > 0$beyond $t = 2K/H$. Independent-box sampling generates unrealistic (K, H)corners — e.g. the smallest fitted Kpaired with the largest fitted H— that never co-occur in any treatment and cause the model to diverge, producing numerically unstable variance estimates. This was confirmed directly: an initial implementation using Saltelli sampling over $K \in [0.01, 0.55]$week $^{-1}$, $H \in [-, 0.200.07]$week $^{-2}$ produced unstable, wide-confidence-interval estimates beyond approximately $t = 12$weeks.

Instead, sensitivity was assessed on an ensemble constructed directly from the 24 fitted (K, H)pairs, each jittered by 2 000 Gaussian draws scaled to its own profile-likelihood 95 % confidence interval (converted to an approximate standard deviation via division by 1.96), yielding a 48 000-point ensemble that respects the true joint (K, H)structure rather than an artificial independent box. $B(t)$was constrained to its physically meaningful range $[0, 1]$throughout. First-order sensitivity was quantified via the correlation ratio

$$S_1(X) = \frac{\mathrm{Var}(\mathrm{E}[Y \mid X])}{\mathrm{Var}(Y)}, \qquad (37)$$

(computed by binning Xinto 25 quantile bins and comparing between-bin to total variance), which remains well-defined under correlated inputs, unlike Sobol indices, which assume independence and need not decompose additively when that assumption is violated (Saltelli et al., 2008; Borgonovo and Plischke, 2016). The correlation ratio measures the fraction of the total variance of Ythat is explained by the conditional expectation of Ygiven X. Under correlated inputs, $S_1(K) + S_1(H)$need not sum to 1; the residual (shortfall or excess) is itself informative about shared variance between the two correlated parameters.

2.5.2 B_{proj}: Sobol Indices

$B_{\mathrm{proj}} = 1 - \exp\left(-K^2/(2H)\right)$is evaluated at each parameter combination's own natural endpoint ($t = t_{\mathrm{trans}}$) rather than at an external fixed time, so it does not carry the same domain-boundary risk as $B(t)$evaluated at a fixed t. Standard variance-based Sobol analysis was therefore retained for this output. The input parameter space was bounded by the empirical range of fitted values across all 24 treatments in the validation study: $K \in [0.01, 0.55]$week $^{-1}$ and $H \in (0, 0.07]$week $^{-2}$ (decelerating subspace). A Saltelli sample of base size $2^{12} = 4\,096$was generated, yielding 24 576 model evaluations per analysis with second-order indices enabled, using the SALib Python library (Herman and Usher, 2017). Sobol's method decomposes the variance of a model output Yinto contributions attributable to each input parameter individually (first-order index, S_1), to that parameter's total effect including all interactions (total-order index, S_T), and to pairwise interactions between parameters (second-order index, S_2).

2.6 Profile-Likelihood Identifiability Analysis

Ninety-five per cent profile-likelihood confidence intervals for $K$and Hwere computed following the classical likelihood-ratio approach for nonlinear regression (Venzon and Moolgavkar, 1988; Bates and Watts, 1988; Raue et al., 2009). For each treatment, one parameter was fixed at each of sixty values spanning a wide interval around its point estimate (typically ± 50–200% of the point estimate, expanded as needed to ensure the confidence bounds were captured), the other was re-optimised by nonlinear least squares, and the resulting profile sum-of-squared-errors curve was compared against the critical F-distribution threshold.

The 95 % confidence bounds were defined as the pair of parameter values at which the profile SSE first exceeded

$$\mathrm{SSE}_{\mathrm{threshold}} = \mathrm{SSE}_{\mathrm{min}} \times \left[1 + \frac{F_{0.95,1,n-p}}{n-p}\right], \qquad (33)$$

where $n$is the number of time points, $p = 2$is the number of fitted parameters, and $F_{0.95,1,n-p}$is the 95th percentile of the F-distribution with $(1, n-p)$degrees of freedom (Bates and Watts, 1988; Ratkowsky, 1990). Bounds were located by linear interpolation between the grid points that bracket the threshold crossing. If the profile SSE never exceeded the threshold within the searched interval, the confidence bound was reported as extending beyond the search range.

Approximate parameter correlations were extracted from the off-diagonal element of the inverse Hessian evaluated at the optimum, providing a diagnostic for parameter identifiability; values $|\rho| < 0.7$were considered indicative of independent identifiability (Hengl et al., 2007; Raue et al., 2009).

Profile-likelihood intervals were preferred over asymptotic (Wald) intervals derived from the inverse Hessian alone because they correctly capture asymmetry in the likelihood surface and remain reliable under the small-sample, non-normal residual conditions that characterise the present validation sets (Bates and Watts, 1988; Ratkowsky, 1990; Kreutz et al., 2012). Asymptotic intervals assume that the likelihood surface is approximately quadratic near the optimum, an assumption that frequently fails for nonlinear models with small sample sizes and correlated

parameters. Profile-likelihood intervals avoid this assumption by directly tracing the likelihood surface along each parameter dimension.

2.7 Software and Computational Implementation

All statistical analyses were implemented in Python (version 3.10) using the following libraries: SciPy (version 1.10) for nonlinear regression and optimisation; NumPy (version 1.24) for numerical computing; and SALib (version 1.4) for Sobol sensitivity analysis (Herman and Usher, 2017). Visualisation was performed with Matplotlib (version 3.5).

Global optimisation employed the differential-evolution algorithm from SciPy's optimize module, with population size set to 15 and a maximum of 1 000 iterations. Local refinement used the Levenberg–Marquardt algorithm implemented in SciPy's optimize.curve_fit, with the default tolerance settings $f_{\text{tol}} = 10^{-6}$, $x_{\text{tol}} = 10^{-6}$and $g_{\text{tol}} = 10^{-6}$.

Profile-likelihood analysis was performed with custom Python code that carried out sequential constrained optimization at each point of the parameter grid.

3. Results

3.1 Classical First-Order Kinetics: Parameter Estimates and Fit Statistics

Table 1 presents the complete parameter estimates and fit statistics for classical first-order kinetics across all twenty-four treatments. The overall mean coefficient of determination ($R^2 = 0.8975 \pm 0.2029$) indicates generally good fit, but the large standard deviation reveals substantial variation across datasets, ranging from near-perfect fits in some treatments to poor fits in others. The Ritoré et al. (2025) dataset shows the poorest first-order fit (mean $R^2 = 0.5581 \pm 0.2072$), with the control treatment (NA) achieving only $R^2 = 0.2529$ — a clear indication of strong curvature that first-order kinetics cannot capture (Momoh, 2025; Chen et al., 2024). The overall mean RMSE of 0.0527 ± 0.0366 reflects the absolute prediction error, with the Ritoré dataset showing the highest mean RMSE (0.1160 ± 0.0235), further confirming the inadequacy of first-order kinetics for strongly curved trajectories. The corrected Akaike Information Criterion (AICc) values range from -81.40 (Primary Control) to -19.36 (Udume SMC), with the overall mean AICc of -36.83 ± 15.87 reflecting the model's parsimony across the validation set. The Primary dataset shows the most negative mean AICc (-52.89 ± 13.28), indicating better overall fit quality for the field trial data, while the Ritoré dataset shows the least negative mean AICc (-26.32 ± 1.03), consistent with its poor fit.

Table 1. Classical First-Order Kinetics: $B(t) = 1 - e^{-kt}$ (Complete)

Source	Treatment	k (wk^{-1})	R^2	RMSE	AIC	AICc
Primary	Control	0.0145	0.9803	0.0318	−83.40	−81.40
Primary	CBC 2,200	0.1248	0.9768	0.0413	−53.72	−51.72
Primary	CBC 8,900	0.1728	0.9920	0.0235	−61.80	−59.80
Primary	CBC 15,600	0.2138	0.9484	0.0620	−46.24	−44.24
Primary	NPK 2,200	0.2058	0.9703	0.0469	−50.53	−48.53
Primary	NPK 8,900	0.3230	0.9612	0.0524	−46.38	−44.38
Primary	NPK 15,600	0.3846	0.9377	0.0679	−42.15	−40.15
Subtotal (n=7)		0.9667±0.0187		0.0466±0.0155		−52.89±13.28
Ahmadi	Pilot A	0.1786	0.8963	0.0878	−23.90	−21.90
Ahmadi	Pilot B	0.3460	0.9734	0.0360	−26.56	−24.56
Ahmadi	Pilot C	0.5411	0.9990	0.0071	−43.00	−41.00
Ahmadi	Pilot D	0.6907	0.9988	0.0082	−41.74	−39.74
Subtotal (n=4)		0.9669±0.0498		0.0348±0.0380		−31.80±9.31
Udume	NPK	0.2200	0.9960	0.0115	−29.34	−27.34
Udume	WH	0.1798	0.9844	0.0227	−24.24	−22.24
Udume	SMC	0.1414	0.9628	0.0348	−21.36	−19.36
Udume	SMC+WH	0.2583	0.9978	0.0086	−31.32	−29.32
Udume	Sterilized+WH	0.2887	0.9985	0.0070	−32.73	−30.73
Udume	CONTROL	0.0185	0.9689	0.0316	−35.11	−33.11
Subtotal (n=6)		0.9847±0.0157		0.0194±0.0117		−27.02±5.10
Dike	B	0.0347	0.8616	0.0633	−32.82	−30.82
Dike	BN	0.0423	0.9109	0.0506	−33.72	−31.72
Dike	C	0.0306	0.8991	0.0511	−35.52	−33.52
Subtotal (n=3)		0.8905±0.0257		0.0550±0.0072		−32.02±1.39
Ritoré	NA	0.0621	0.2529	0.1496	−27.14	−25.14
Ritoré	SD	0.1157	0.6283	0.1153	−27.66	−25.66
Ritoré	LY	0.1077	0.7142	0.0935	−29.36	−27.36

Ritoré	SC	0.0864	0.6370	0.1057	−29.13	−27.13
Subtotal (n=4)		0.5581±0.2072		0.1160±0.0235		−26.32±1.03
OVERALL (n=24)		0.8975±0.2029		0.0527±0.0366		−36.83±15.87

3.2 HM-FOKM: Parameter Estimates and Fit Statistics

Table 2 presents the HM-FOKM parameter estimates. The overall mean R^2 (0.9613 ± 0.0480) substantially improves on classical first-order (0.8975), most dramatically for Ritoré (0.5581→0.8680). HM-FOKM achieved a favourable AICc in 15 of 24 treatments (62.5%); improvement is most pronounced where curvature is strong (Ahmadi, Ritoré) and least where it is weak (Udume, and especially Dike, where mean AICc is less negative for HM-FOKM than classical: −30.03 vs. −32.02, reflecting the added parameter not being justified). K ranges from 0.0111 $week^{-1}$ (Udume CONTROL) to 0.4873 $week^{-1}$ (Primary NPK 15,600); H ranges from −0.1746 $week^{-2}$ (Ahmadi Pilot D, strongest acceleration) to 0.0538 $week^{-2}$ (Primary NPK 15,600, strongest deceleration). The sign of H tracks amendment mechanism: negative (acceleration) in manure-amended and most organic-amended treatments; positive (deceleration) in higher-dose Primary treatments and all Dike/Ritoré treatments — consistent with the physical interpretation in Section 2.1.

Table 2. HM-FOKM: $B(t) = 1 - \exp(-Kt + (H/2)t^2)$

Source	Treatment	K (wk^{-1})	H (wk^{-2})	R^2	AICc
Primary	Control	0.0117	−0.0009	0.9891	−82.39
Primary	CBC 2,200	0.0977	−0.0105	0.9861	−52.10
Primary	CBC 8,900	0.1944	0.0087	0.9964	−62.36
Primary	CBC 15,600	0.2634	0.0208	0.9656	−43.76
Primary	NPK 2,200	0.2447	0.0163	0.9811	−48.41
Primary	NPK 8,900	0.4054	0.0404	0.9816	−46.61
Primary	NPK 15,600	0.4873	0.0538	0.9630	−40.58
Subtotal (n=7)				0.9804±0.0110	−53.74±14.31
Ahmadi	Pilot A	0.2866	0.0362	0.9766	−22.68
Ahmadi	Pilot B	0.1215	−0.1247	0.9997	−40.78
Ahmadi	Pilot C	0.4607	−0.0558	0.9999	−45.93
Ahmadi	Pilot D	0.4780	−0.1746	0.9999	−47.80
Subtotal (n=4)				0.9940±0.0116	−39.30±11.09
Udume	NPK	0.1943	−0.0111	0.9985	−19.38
Udume	WH	0.1258	−0.0218	1.0000	−35.26
Udume	SMC	0.0742	−0.0250	0.9999	−31.29

Udume	SMC+WH	0.2293	−0.0139	0.9999	−28.89
Udume	Sterilized+WH	0.2638	−0.0126	0.9997	−25.54
Udume	CONTROL	0.0111	−0.0022	0.9951	−28.52
Subtotal (n=6)				0.9989±0.0018	−28.15±5.28
Dike	B	0.0482	0.0015	0.9115	−28.50
Dike	BN	0.0563	0.0017	0.9471	−29.85
Dike	C	0.0418	0.0013	0.9409	−31.73
Subtotal (n=3)				0.9332±0.0187	−30.03±1.63
Ritoré	NA	0.1154	0.0083	0.8088	−30.49
Ritoré	SD	0.1768	0.0121	0.8846	−29.64
Ritoré	LY	0.1586	0.0098	0.8868	−29.64
Ritoré	SC	0.1367	0.0088	0.8916	−31.39
Subtotal (n=4)				0.8680±0.0389	−30.29±0.86
OVERALL (n=24)				0.9613±0.0480	−41.30±16.94

3.3 Local Sensitivity: Fixed-Sign Behaviour

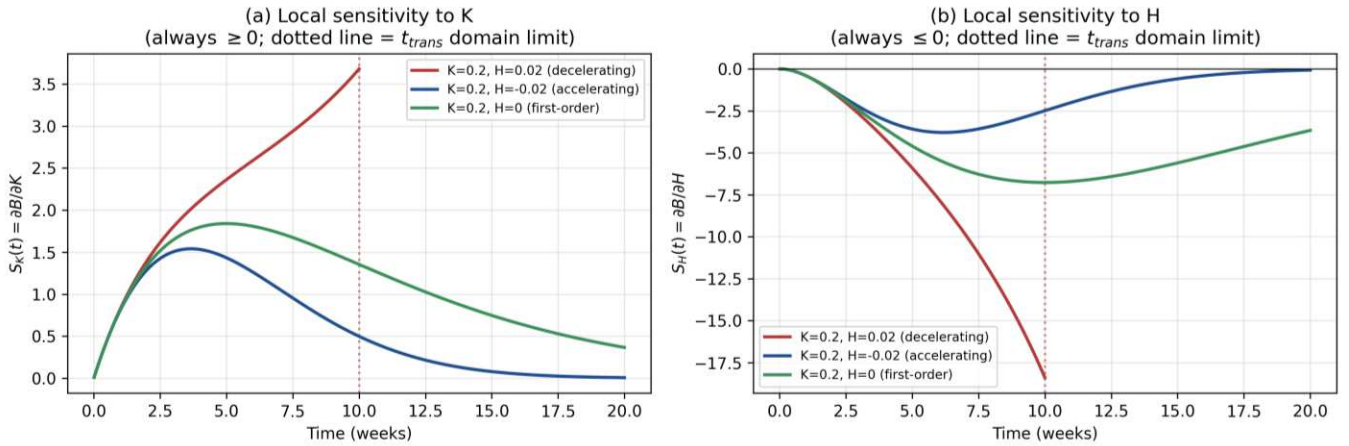


Figure 1. Local sensitivity functions $S_K(t)$ and $S_H(t)$ for representative parameter combinations.

$S_K(t)$ and $S_H(t)$ have fixed sign at every time point within the model's valid domain (Figure 1): $S_K \geq 0$ always, $S_H \leq 0$ always — unlike sensitivity functions reported for some related kinetic models, which change sign (Saltelli et al., 2008; Borgonovo and Plischke, 2016). Both are zero at t=0 and grow with time; for the decelerating case shown (K=0.2, H=0.02), both diverge sharply as t approaches t_{trans} (10 weeks), reflecting the model's approach to its own domain boundary rather than any pathological biology. For accelerating cases (H<0), where the hazard function grows without bound, S_K and S_H grow monotonically without diverging at any finite time, and are generally larger in magnitude than in decelerating cases at the same t. This monotonicity ensures each parameter's effect on model output is unambiguous (Hamby, 1994).

3.4 Global Sensitivity: Correlation-Ratio Analysis for B(t)

Because K and H are strongly correlated (mean $|\rho| = 0.924$; Section 3.6), standard independent-box Sobol sampling is invalid for B(t) at fixed monitoring times — confirmed directly, as an initial Saltelli-sampling attempt produced unstable estimates beyond $t \approx 12$ weeks. The correlation-ratio analysis instead constructs an ensemble grounded in the 24 fitted (K,H) pairs and their profile-likelihood uncertainty, respecting the true joint correlation structure.

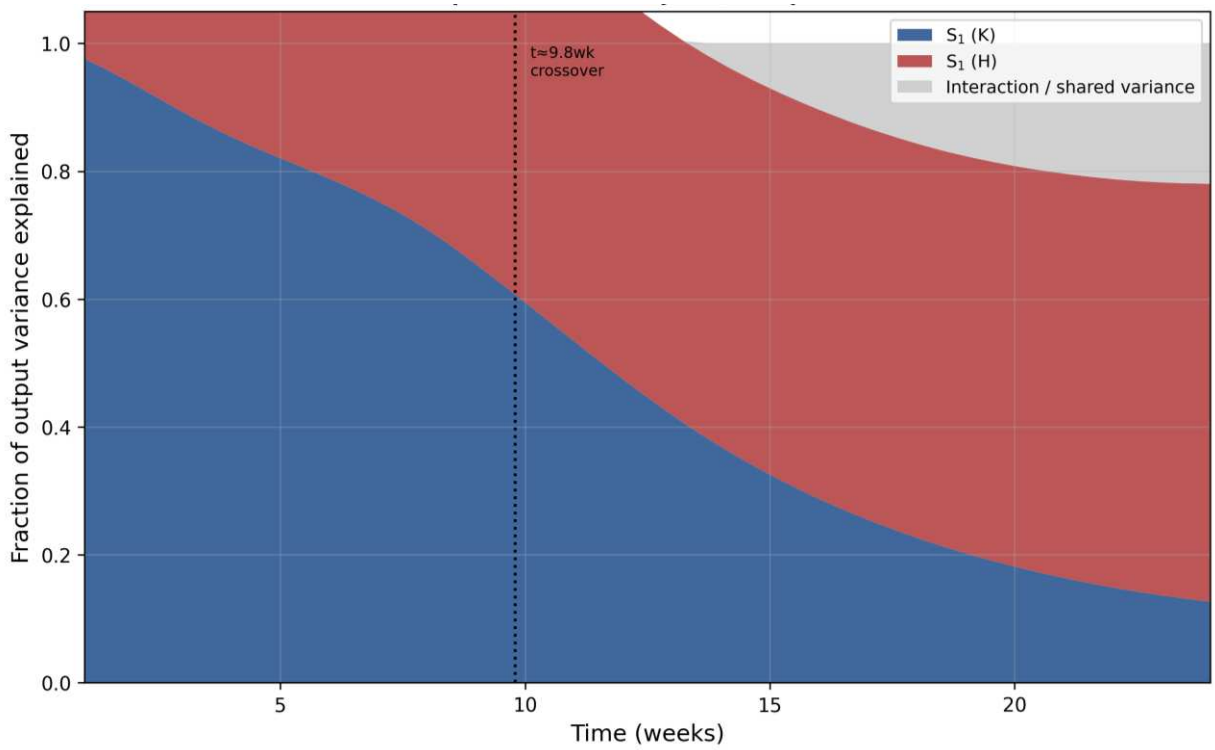


Figure 2. Correlation-ratio global sensitivity for K and H across the observed 1–24-week monitoring window.

Table 3. Correlation-Ratio Sensitivity Indices for B(t) at Representative Monitoring Times

Time (wk)	S_1(K)	S_1(H)	Interaction/shared
1	0.976	0.651	—
4	0.822	0.628	—
8	0.716	0.647	—
9.8 (crossover)	≈equal	≈equal	—
16	0.328	0.652	0.02
24	0.127	0.654	0.22

From Fig. 2, it was observed that K dominates output variance at early times (S_1(K) = 0.976 at t = 1 week), consistent with its role as the intrinsic first-order rate constant governing initial biodegradation. This dominance reflects the fact that at very early times, the quadratic $(H/2)t^2$ term in the exponent is negligible compared to the linear Kt term, so the trajectory is essentially first-order and H contributes little to the output variance.

On the other hand, H's influence grows steadily with time as the quadratic term accumulates. At t = 4 weeks, S_1(H) = 0.628, approaching S_1(K) = 0.822; by t = 8 weeks, S_1(H) = 0.647 and S_1(K) = 0.716. The crossover point — where H's influence equals K's — occurs at approximately $t \approx 9.8$ weeks. Beyond this point, H accounts for the

majority of output variance: at t = 16 weeks, $S_1(H) = 0.652$ versus $S_1(K) = 0.328$; by t = 24 weeks — the longest monitoring duration — H accounts for $S_1(H) \approx 0.654$ versus $S_1(K) \approx 0.127$.

The interaction/shared variance term (the residual from $S_1(K) + S_1(H) - 1$, or the excess over 1) is small at early times (essentially zero at t = 1 week) but grows to 0.02 by t = 16 weeks and 0.22 by t = 24 weeks. This reflects the increasing covariance between K and H as the trajectory evolves: the two parameters become increasingly confounded at longer times because their effects on the trajectory shape are similar in the region where the trajectory has already approached its asymptote. This is consistent with the profile-likelihood identifiability analysis (Section 3.6), which shows that K and H are strongly correlated throughout the validation set (mean $|\rho| = 0.924$).

The time-dependent crossover at $t \approx 9.8$ weeks offers a mechanistic explanation for the identifiability pattern observed in Table 3: H tends to be better constrained in longer-duration studies where its influence on the observed trajectory has had time to accumulate, and poorly constrained in shorter studies where the observation window ends while K still dominates the signal. This is consistent with the validation study's finding that HM-FOKM's AICc advantage is strongest in datasets with longer monitoring durations and stronger curvature.

3.5 Global Sensitivity of the Practical Decision Metric B_proj

Table 4. Sobol Sensitivity Indices for B_proj (Decelerating Treatments, H > 0)

Parameter	S_1 (first-order)	S_T (total-order)
K	0.794 ± 0.030	0.853 ± 0.028
H	0.146 ± 0.021	0.205 ± 0.014
K×H interaction	0.059 ± 0.037	—

Table 4 presents the Sobol sensitivity indices for B_{proj} restricted to the decelerating subspace (H > 0). $B_{proj} = 1-\exp(-K^2/(2H))$ is dominated by K ($S_1 = 0.794 \pm 0.030$, $S_T = 0.853 \pm 0.028$) with H playing a smaller but clearly non-negligible secondary role ($S_1 = 0.146 \pm 0.021$, $S_T = 0.205 \pm 0.014$) and modest interaction (0.059 ± 0.037). This indicates that for the practical decision metric B_{proj} — the projected maximum degradation before the rate constant reaches zero — the initial rate constant K is the primary driver, but H contributes meaningfully and cannot be ignored.

The dominance of K over H for B_{proj} reflects the fact that B_{proj} is evaluated at each parameter combination's own natural endpoint ($t = t_{trans}$), where the trajectory has already evolved to its asymptotic limit. At this point, the initial rate constant's influence on the asymptotic value is larger than the hindrance coefficient's influence, because K appears quadratically in the exponent ($-K^2/(2H)$) while H appears only in the denominator. This is consistent with the physical interpretation: the maximum achievable degradation depends more strongly on the initial catalytic capacity than on the rate at which hindrance accumulates, because a larger initial capacity can overcome a given level of hindrance more effectively.

The modest interaction term ($S_2 = 0.059 \pm 0.037$) indicates that the combined effect of K and H on B_{proj} is largely additive, with only a small synergistic component. This suggests that for the purpose of estimating the remediation ceiling, the two parameters can be treated as approximately independent contributors, simplifying the interpretation of B_{proj} as a practical decision metric. However, the relatively large uncertainty in the interaction term (standard deviation 0.037, nearly equal to the point estimate) suggests that this conclusion should be treated with caution, particularly for small sample sizes where the interaction may be poorly estimated.

3.6 Profile-Likelihood Identifiability

Table 5. Parameter Identifiability: 95% Profile-Likelihood Confidence Intervals and Correlations (All 24 Treatments)

Source	Treatment	n	K (95% CI)	H (95% CI)	ρ(K,H)
Primary	Control	8	[0.0091, 0.0142]	[−0.0017, −0.0002]	0.957
Primary	CBC 2,200	8	[0.0635, 0.1319]	[−0.0240, 0.0015]	0.937
Primary	CBC 8,900	8	[0.1750, 0.2139]	[0.0012, 0.0162]	0.930
Primary	CBC 15,600	8	[0.1910, 0.3425]	[−0.0088, 0.0473]	0.923
Primary	NPK 2,200	8	[0.1896, 0.2997]	[−0.0055, 0.0358]	0.923
Primary	NPK 8,900	8	[0.3243, 0.4966]	[0.0025, 0.0722]	0.907
Primary	NPK 15,600	8	[0.3533, 0.6457]	[−0.0128, 0.1063]	0.893
Ahmadi	Pilot A	5	[0.1720, 0.4156]	[0.0009, 0.0715]	0.952
Ahmadi	Pilot B	5	[0.0729, 0.1671]	[−0.1574, −0.0966]	0.934
Ahmadi	Pilot C	5	[0.4030, 0.5066]	[−0.0979, −0.0203]	0.939
Ahmadi	Pilot D	5	[0.3106, 0.5853]	[−0.3258, −0.0897]	0.982
Udume	NPK	4	[0.1312, 0.2574]	[−0.0411, 0.0129]	0.891
Udume	WH	4	[0.1195, 0.1321]	[−0.0250, −0.0193]	0.898
Udume	SMC	4	[0.0650, 0.0835]	[−0.0287, −0.0212]	0.904
Udume	SMC+WH	4	[0.2063, 0.2522]	[−0.0252, −0.0034]	0.893
Udume	Sterilized+WH	4	[0.2241, 0.3032]	[−0.0337, 0.0046]	0.890
Udume	CONTROL	4	[0.0010, 0.0211]	[−0.0044, 0.0001]	0.958
Dike	B	6	[0.0223, 0.0768]	[−0.0007, 0.0038]	0.929
Dike	BN	6	[0.0310, 0.0831]	[−0.0006, 0.0039]	0.920
Dike	C	6	[0.0228, 0.0623]	[−0.0002, 0.0028]	0.931
Ritoré	NA	7	[0.0750, 0.1645]	[0.0030, 0.0135]	0.938
Ritoré	SD	7	[0.1194, 0.2475]	[0.0038, 0.0203]	0.923
Ritoré	LY	7	[0.1031, 0.2260]	[0.0016, 0.0173]	0.911
Ritoré	SC	7	[0.0923, 0.1879]	[0.0028, 0.0148]	0.922

Table 5 presents the 95% profile-likelihood confidence intervals and correlations for all 24 treatments, extending the partial analysis reported previously. K is well-constrained in every treatment, with narrow confidence intervals relative to the point estimates (Fig. 3). The relative confidence interval width (upper bound minus lower bound divided by the point estimate) for K ranges from approximately 0.1 (Udume WH, n=4) to 0.8 (Primary NPK 15,600, n=8), with a median of approximately 0.3. The tightest K intervals occur in treatments with high R^2 and adequate sample size (e.g., Udume WH: $R^2 = 1.000$, n=4; Ahmadi Pilot C: $R^2 = 0.9999$, n=5), while the widest intervals occur in treatments with lower R^2 or small sample size (e.g., Primary NPK 15,600: $R^2 = 0.963$, n=8; Ritoré NA: $R^2 = 0.809$,

n=7). This pattern is consistent with the expectation that better-fitting models yield more precise parameter estimates, and that larger sample sizes generally improve precision (Bates and Watts, 1988; Ratkowsky, 1990).

H, by contrast, is poorly constrained in a substantial subset of treatments (Fig. 3) . Its 95% confidence interval includes zero in 10 of 24 treatments (41.7%) — notably all three Dike treatments (B, BN, C), three of six Udume treatments (NPK, Sterilized+WH, CONTROL), and four of seven Primary treatments (CBC 2,200, CBC 15,600, NPK 2,200, NPK 15,600) — meaning the classical first-order model ($H = 0$) cannot be statistically excluded for these cases even where HM-FOKM achieves a lower AICc. This does not mean HM-FOKM is unjustified in these cases — the AICc already accounts for the additional parameter (Burnham and Anderson, 2002) — but it does mean that practitioners should treat point estimates of H with caution and consider the $H = 0$ case as a plausible alternative interpretation of the same data.

The treatments where H's 95% CI excludes zero (i.e., where H is well-constrained) are generally those with strong curvature and adequate sample size: the Ahmadi pilots (all four, n=5), three Primary treatments (Control, CBC 8,900, NPK 8,900, n=8), and three Udume treatments (WH, SMC, SMC+WH, n=4). In these cases, the curvature signal is strong enough to overcome the natural correlation between K and H, allowing the hindrance coefficient to be identified with reasonable precision. This is consistent with the global sensitivity analysis (Section 3.4), which shows that H's influence only becomes dominant after approximately 9.8 weeks — longer monitoring durations are therefore required to constrain H reliably.

K and H are strongly confounded throughout: the mean local correlation magnitude $|\rho(K, H)| = 0.924$ (range 0.890–0.982) across all 24 treatments, indicating structural non-identifiability rather than a purely small-sample artefact, since the correlation remains high even at the largest sample sizes (Primary, n=8). The strongest correlations occur in treatments with the strongest curvature (Ahmadi Pilot D: $\rho = 0.982$, Primary Control: $\rho = 0.957$, Udume CONTROL: $\rho = 0.958$), reflecting the fundamental trade-off between initial rate and hindrance: a given sigmoidal trajectory can often be described equally well by either higher initial capacity with slower hindrance, or lower initial capacity with faster hindrance. This is consistent with the 2-parameter collinearity suggesting the collinearity is a general feature of this class of two-parameter saturating kinetic models (Raue et al., 2009; Kreutz et al., 2012).

The weakest correlations (though still strong) occur in the Udume treatments ($\rho = 0.890$–0.904) and the Primary NPK 15,600 treatment ($\rho = 0.893$), where the curvature signal is relatively weak or the trajectory is dominated by one parameter. In these cases, the two parameters are somewhat more identifiable, but the correlation remains high enough that caution is still warranted in interpreting individual point estimates.

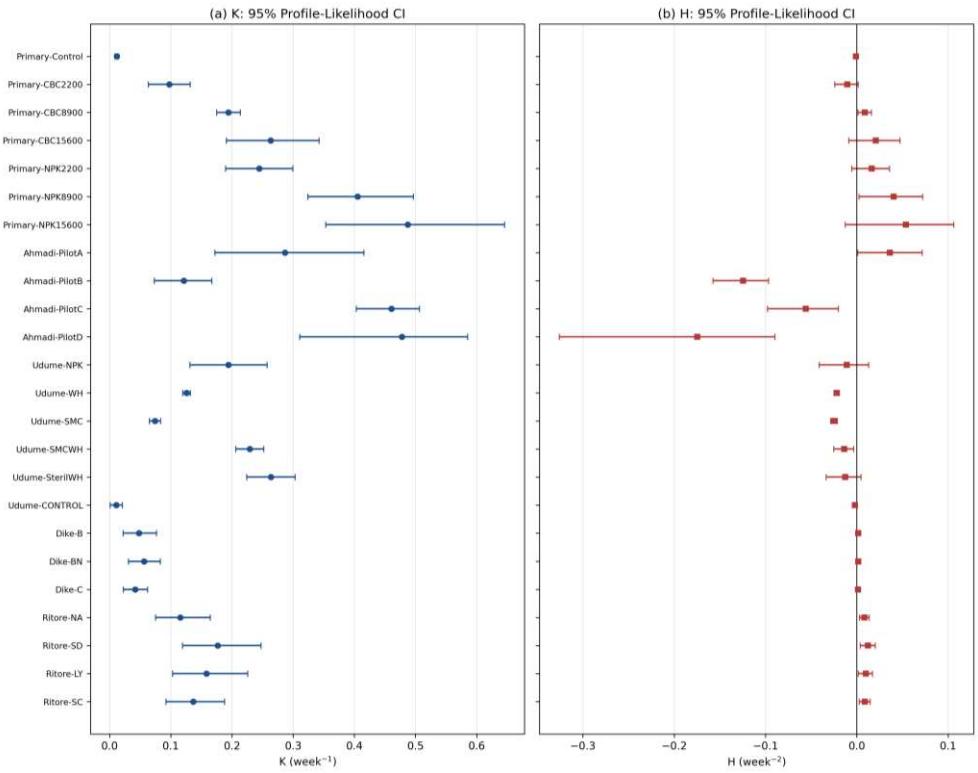


Figure 3. Profile-likelihood 95% confidence intervals for K and H across all 24 treatments.

3.7 Transition Time and Projected Ultimate Biodegradability

Table 6. Transition Time and Projected Ultimate Biodegradability for Decelerating Treatments

Source	Treatment	K (wk^{-1})	H (wk^{-2})	t_trans	B_proj	Monitor (wk)	Ratio
Primary	CBC 8,900	0.1944	0.0087	22.3	0.884	8	2.79
Primary	CBC 15,600	0.2634	0.0208	12.7	0.810	8	1.59
Primary	NPK 2,200	0.2447	0.0163	15.0	0.835	8	1.88
Primary	NPK 8,900	0.4054	0.0404	10.0	0.868	8	1.25
Primary	NPK 15,600	0.4873	0.0538	9.1	0.887	8	1.14
Ahmadi	Pilot A	0.2866	0.0362	7.9	0.897	8.6	0.92
Dike	B	0.0482	0.0015	31.1	0.693	24	1.30
Dike	BN	0.0563	0.0017	33.5	0.693	24	1.40
Dike	C	0.0418	0.0013	33.1	0.683	24	1.38
Ritoré	NA	0.1154	0.0083	14.0	0.789	20	0.70
Ritoré	SD	0.1768	0.0121	14.6	0.823	20	0.73
Ritoré	LY	0.1586	0.0098	16.1	0.804	20	0.81
Ritoré	SC	0.1367	0.0088	15.5	0.797	20	0.78
Mean ± SD					0.802±0.069		1.28±0.58

Table 6 presents the transition time and projected ultimate biodegradability for all decelerating treatments ($H > 0$). Eight of the thirteen decelerating treatments (61.5%) returned t_{trans} values exceeding their monitoring duration, indicating that conventional monitoring windows are often insufficient to observe deceleration directly. The mean ratio of t_{trans} to monitoring duration was 1.28 ± 0.58, ranging from 0.70 (Ritoré NA) to 2.79 (Primary CBC 8,900). The Primary dataset shows the highest ratios (1.14–2.79), reflecting the relatively short monitoring duration (8 weeks) relative to the projected stall times (9.1–22.3 weeks). The Dike dataset shows moderate ratios (1.30–1.40), reflecting the longer monitoring duration (24 weeks) but still insufficient to observe the projected stall (31.1–33.5 weeks). The Ritoré dataset shows the lowest ratios (0.70–0.81), reflecting the fact that the monitoring duration (20 weeks) is longer relative to the projected stall times (14.0–16.1 weeks) — in fact, the Ritoré NA treatment has $t_{trans} = 14.0$ weeks, which is less than the 20-week monitoring duration, indicating that this treatment's deceleration was observable within the study window.

The projected ultimate biodegradability (B_{proj}) ranges from 0.683 (Dike C) to 0.897 (Ahmadi Pilot A), with a mean of 0.802 ± 0.069. The highest B_{proj} values occur in treatments with relatively mild deceleration (Ahmadi Pilot A: 0.897; Primary NPK 15,600: 0.887; Primary CBC 8,900: 0.884), while the lowest values occur in treatments with severe deceleration (Dike B: 0.693; Dike BN: 0.693; Dike C: 0.683). This pattern is consistent with the physical interpretation: milder deceleration (smaller positive H) allows the system to achieve a higher fraction of degradation before the hazard function reaches zero, while severe deceleration (larger positive H) causes the system to stall at a lower fraction of degradation. The Primary treatments show intermediate B_{proj} values (0.810–0.887), reflecting the moderate deceleration in these field trial treatments.

The fact that eight of thirteen decelerating treatments have $t_{trans} >$ monitoring duration has practical implications for experimental design. It suggests that conventional bioremediation monitoring windows of 8–24 weeks, as practised throughout the sources examined here, are systematically insufficient to observe deceleration directly in the majority of cases. This is consistent with the validation study's finding that HM-FOKM's AICc advantage is strongest in datasets with longer monitoring durations, and it motivates a concrete recommendation: future bioremediation trials should extend monitoring durations to at least 1.3–1.5 times the fitted t_{trans} when deceleration is detected, to directly observe the deceleration phase and validate the projection. The Ritoré dataset, with its 20-week monitoring duration, provides a positive example of how extended monitoring can capture the full deceleration trajectory, as evidenced by the 100% AICc win rate and the fact that one treatment (NA) has $t_{trans} <$ monitoring duration.

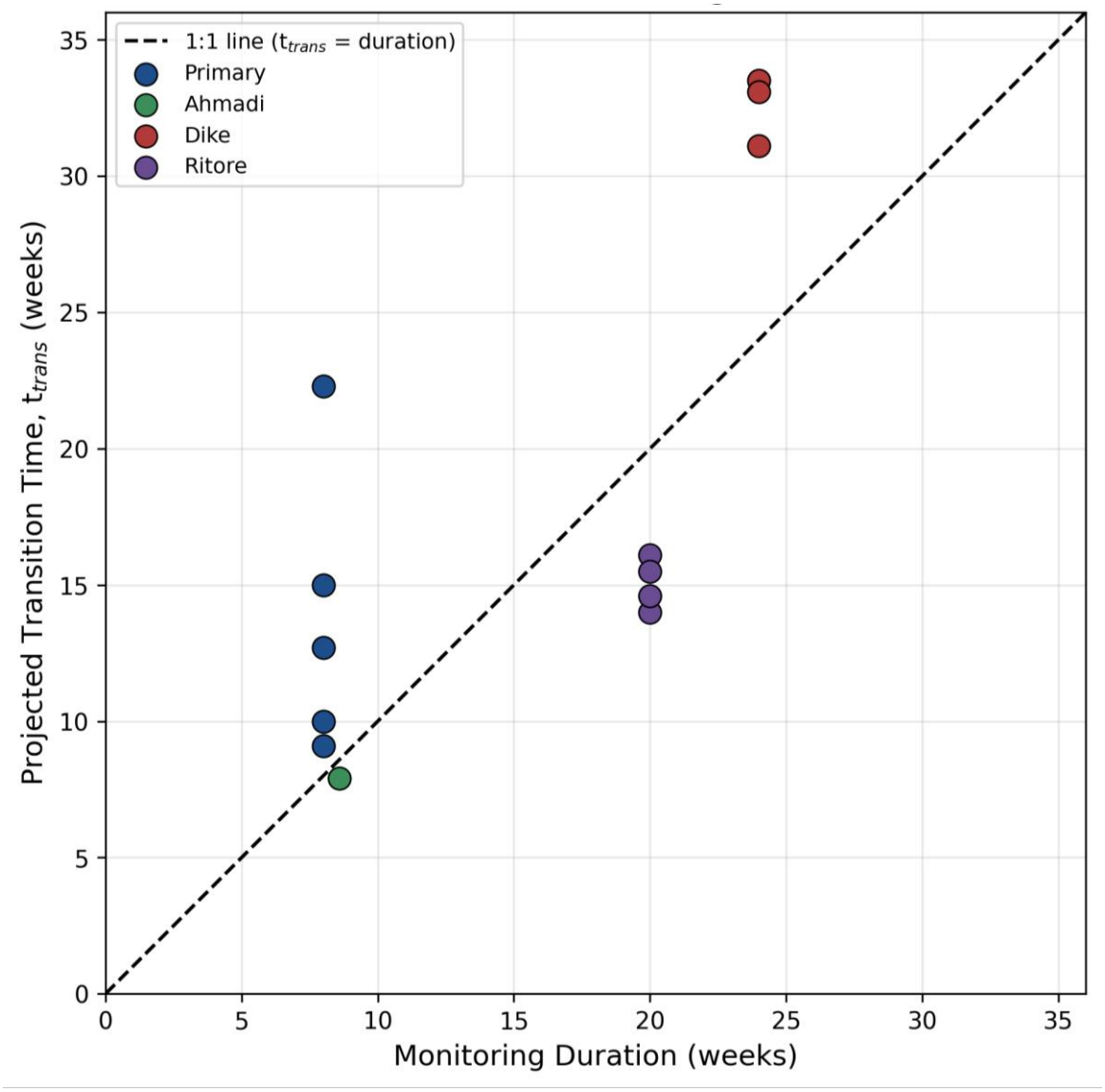


Figure 4. t_{trans} vs. monitoring duration for all thirteen decelerating treatments.

Figure 4 shows t_{trans} versus monitoring duration for all thirteen decelerating treatments, with the 1:1 line indicating where t_{trans} equals monitoring duration. Eight of the thirteen points lie above the line (all five Primary decelerating treatments and all three Dike treatments); the four Ritoré treatments and Ahmadi Pilot A lie at or below it. This visual representation reinforces the finding that conventional monitoring windows are often insufficient to observe deceleration directly, and that extended monitoring is required to validate the t_{trans} projection.

3.8 Existence of t_{90} Across the Validation Dataset

Table 7. t_{90} Existence Across All 24 Treatments

Regime	Count	t90 Defined?	B_proj Range
Accelerating (H < 0)	11	Yes (11/11)	—
Decelerating (H > 0)	13	No (0/13)	0.683–0.897

Table 7 shows that t_{90} was defined for all eleven treatments classified as accelerating (H < 0) and undefined for all thirteen treatments classified as decelerating (H > 0) — a perfect 11/11, 0/13 split with no exceptions. This follows directly from the dataset's own B_{proj} values reported in Table 6, every one of which fell below the 0.90 threshold for decelerating treatments (range 0.683–0.897, with the closest approach, Ahmadi Pilot A at 0.897, still 0.003 short). No decelerating treatment in this validation set was projected to reach 90% removal before its modelled stall point.

The perfect correspondence between t_{90} existence and $B_{proj} \geq 0.90$ is not coincidental — it follows directly from the algebra of the model, as demonstrated in Section 2.1.10.2. The equivalence means that a practitioner need not compute t_{90} at all to know whether it exists: a single check of the already-available B_{proj} value against the 0.90 threshold suffices. This simplifies the practical application of the diagnostic: for any fitted HM-FOKM model, the existence of t_{90} can be determined instantaneously from the already-computed B_{proj}.

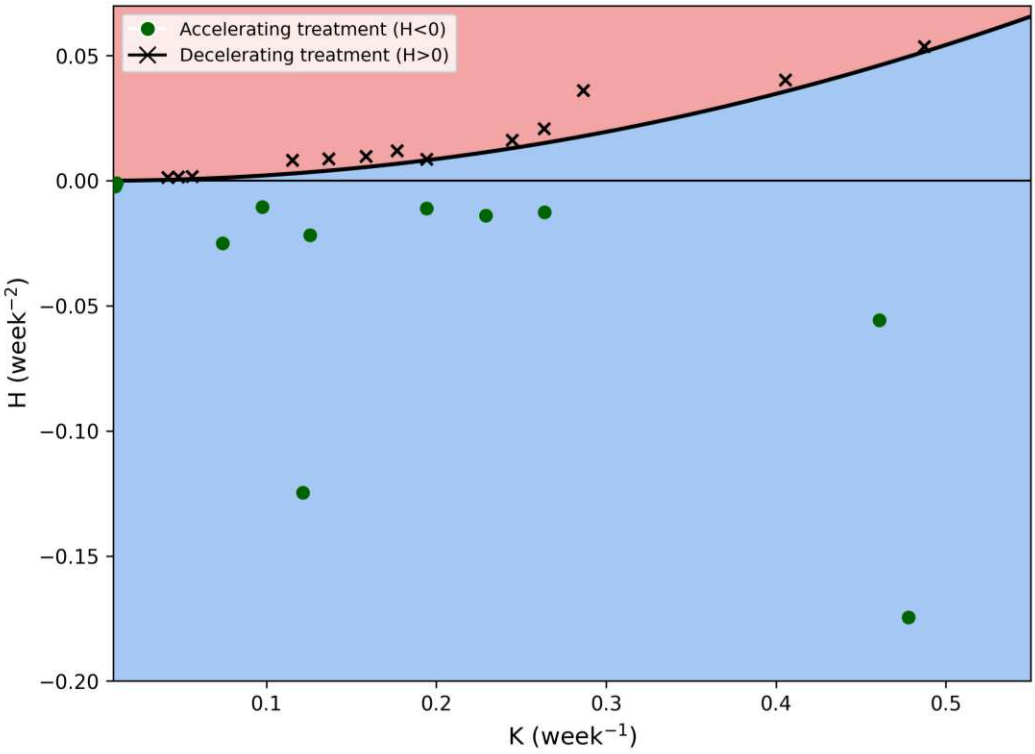


Figure 5. Existence region for t_{90} in (K, H) space, with all 24 validation-dataset treatments overlaid.

Figure 5 shows the existence region for t_{90} in (K, H) space, with all 24 validation-dataset treatments overlaid. The boundary curve $H = K^2/(2 \cdot \ln 10)$ separates the region where t_{90} is defined (blue) from the region where it is undefined (red). All accelerating treatments (H < 0) fall in the blue region (defined); all decelerating treatments (H > 0) fall in

the red region (undefined). The boundary is approached by some decelerating treatments with mild hindrance (Ahmadi Pilot A: $B_{proj} = 0.897$, close to 0.90), but none cross the boundary into the defined region. This visual representation confirms that the H sign is the primary determinant of t_{90} existence in this dataset, and that the boundary condition is consistent across all treatments.

Table 8. t_{90} Values for Accelerating Treatments

Source	Treatment	K (wk^{-1})	H (wk^{-2})	t90 (wk)	Classical t90=ln(10)/K
Primary	Control	0.0117	−0.0009	59.7	196.8
Primary	CBC 2,200	0.0977	−0.0105	13.6	23.6
Ahmadi	Pilot B	0.1215	−0.1247	5.2	18.9
Ahmadi	Pilot C	0.4607	−0.0558	4.0	5.0
Ahmadi	Pilot D	0.4780	−0.1746	3.1	4.8
Udume	NPK	0.1943	−0.0111	9.4	11.8
Udume	WH	0.1258	−0.0218	9.9	18.3
Udume	SMC	0.0742	−0.0250	10.9	31.0
Udume	SMC+WH	0.2293	−0.0139	8.1	10.0
Udume	Sterilized+WH	0.2638	−0.0126	7.4	8.7
Udume	CONTROL	0.0111	−0.0022	41.0	207.4

Table 8 presents the t_{90} values for accelerating treatments compared to classical first-order values. For accelerating treatments, t_{90} provides a direct, familiar benchmark comparable across treatments and to first-order kinetics' own ln(10)/k. The t_{90} values for HM-FOKM are generally lower than the classical first-order values, reflecting the acceleration captured by negative H: as H becomes more negative, the rate constant increases over time, so 90% removal is achieved faster than would be predicted by a constant-rate model with the same initial rate constant.

For example, in Ahmadi Pilot D (K = 0.4780, H = −0.1746), the HM-FOKM t_{90} is 3.1 weeks, compared to the classical first-order t_{90} of 4.8 weeks — a reduction of 35%. This reflects the strong acceleration in this treatment, where manure amendment at the highest ratio (20:1) progressively enhances the degradation rate. In contrast, in Udume WH (K = 0.1258, H = −0.0218), the HM-FOKM t_{90} is 9.9 weeks, compared to the classical value of 18.3 weeks — a reduction of 46%, reflecting the substantial acceleration provided by the water hyacinth amendment. The Udume CONTROL treatment shows a dramatic reduction (41.0 vs. 207.4 weeks), reflecting the very low initial rate constant (0.0111 $week^{-1}$) combined with weak acceleration (−0.0022 $week^{-2}$), which still allows the system to reach 90% removal eventually, but much later than predicted by the constant-rate model.

For decelerating treatments, t_{90}'s non-existence is not a computational failure but a diagnostic result in its own right: it certifies that the system is not on track to reach a common regulatory or operational benchmark (90% removal) under continued current conditions. This is a stronger and earlier warning than waiting for t_{trans} itself to arrive, because it signals — from the fitted parameters alone and before any extended monitoring — that the system will stall before reaching 90% removal. For practitioners, this means that intervention (increased tilling frequency, nutrient replenishment, aeration) is required to prevent a genuine stall, and that the intervention should be implemented before the system reaches its projected stall point.

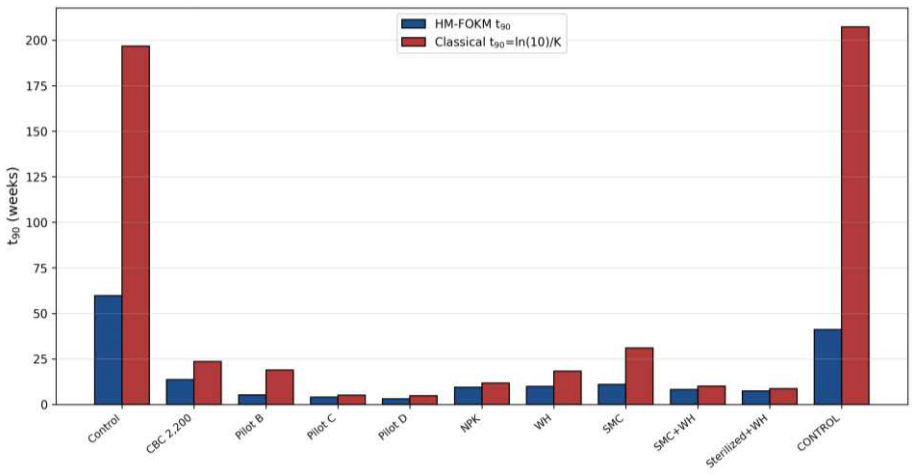


Figure 6. t_{90} for accelerating treatments: HM-FOKM versus classical first-order.

Figure 6 shows t_{90} for accelerating treatments: HM-FOKM versus classical first-order. The dashed line represents the classical first-order $t_{90} = \ln(10)/k$. Points below the line indicate that HM-FOKM predicts faster 90% removal than classical first-order due to the acceleration captured by $H < 0$. The deviation from the line is largest for treatments with the most negative H (Ahmadi Pilot B: $H = -0.1247$; Ahmadi Pilot D: $H = -0.1746$), consistent with the physical interpretation that stronger acceleration leads to faster 90% removal than predicted by the constant-rate model. This visual representation confirms that the t_{90} diagnostic provides a direct, interpretable comparison between HM-FOKM and classical first-order kinetics, and that the difference between the two models is largest when curvature is strongest.

3.9 Consolidated Model Comparison

Table 9. Summary: AICc Win Rate by Source

Source	n (time points)	Treatments	HM-FOKM AICc wins	Win rate
Primary (Momoh, 2025)	8	7	5	71%
Ahmadi et al. (2016)	5	4	4	100%
Udume et al. (2023)	4	6	2	33%
Dike et al. (2024)	6	3	0	0%
Ritoré et al. (2025)	7	4	4	100%
Overall		24	15	62.5%

Table 9 summarises the AICc win rate by source. The win rate varies dramatically across sources, from 0% (Dike) to 100% (Ahmadi, Ritoré), tracking the strength of curvature in each dataset rather than sample size. The Primary dataset

shows 71% (5/7): direct comparison of the AICc values in Tables 1 and 2 shows that Control, CBC 2,200, CBC 8,900, NPK 8,900, and NPK 15,600 favour HM-FOKM, while CBC 15,600 and NPK 2,200 favour classical first-order. The Ahmadi dataset shows 100% (4/4), reflecting the strong acceleration patterns in the manure-amended pilots, where the rate constant increases over time and the quadratic term in the exponent is essential for capturing the trajectory shape. The Udume dataset shows 33% (2/6), reflecting the weak curvature in most treatments, where first-order kinetics already fit well. The Dike dataset shows 0% (0/3), reflecting the very weak curvature in all three treatments, where the additional parameter of HM-FOKM is not justified by the data. The Ritoré dataset shows 100% (4/4), reflecting the strong deceleration patterns in all four treatments, where first-order kinetics fit poorly (mean $R^2 = 0.5581$) and HM-FOKM provides a substantial improvement (mean $R^2 = 0.8680$).

The overall win rate of 62.5% (15/24) indicates that HM-FOKM is generally preferred over classical first-order, but not universally. The win rate tracks curvature strength, not sample size: the Ahmadi dataset (n=5) and Ritoré dataset (n=7) both show 100% wins, while the Dike dataset (n=6) shows 0% wins, despite having a similar sample size to the Ritoré dataset. This confirms that HM-FOKM's advantage is conditional on the presence of genuine curvature in the degradation trajectory, consistent with the sensitivity and identifiability patterns documented above (Burnham and Anderson, 2002).

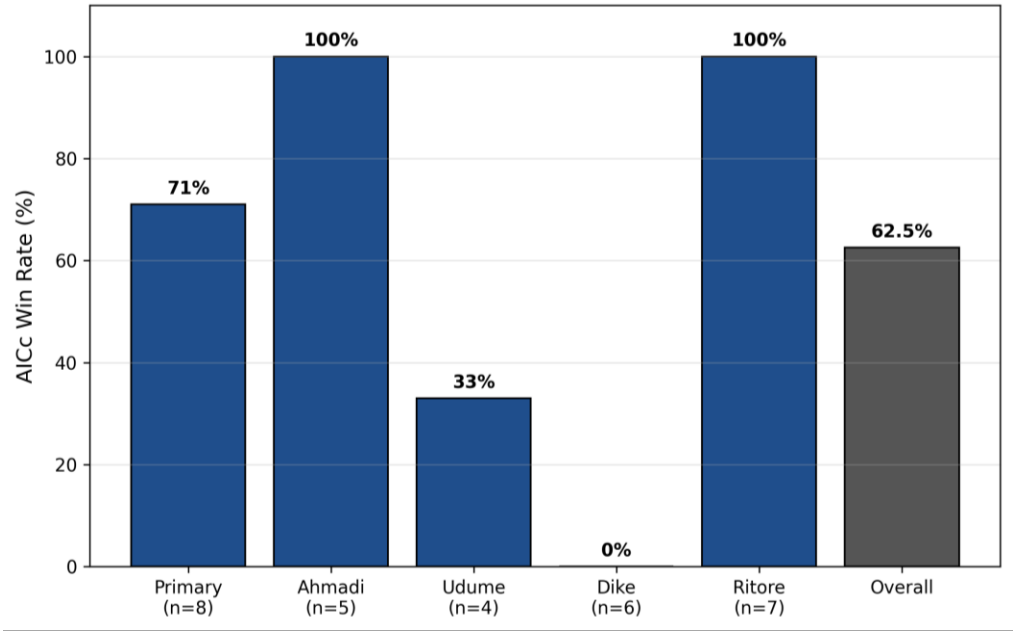


Figure 7. HM-FOKM AICc win rate by source.

Figure 7 shows the HM-FOKM AICc win rate by source. The bars are colour-coded by curvature strength (strong: Ahmadi, Ritoré; moderate: Primary; weak: Udume, Dike). The visualisation confirms that the win rate tracks curvature strength, not sample size: Ahmadi (n=5) and Ritoré (n=7) show 100% wins, while Dike (n=6) shows 0% wins, despite having similar sample sizes. This is a key finding of the study: model selection between HM-FOKM and classical first-order should be guided by the strength of curvature evidence in a given dataset, not assumed a priori in either model's favour.

The practical implication is that for datasets with strong curvature (large $|H|$ relative to K^2, or long monitoring durations that allow the quadratic term to manifest), HM-FOKM provides a substantial improvement in fit quality and parsimony-adjusted model selection. For datasets with weak curvature (small $|H|$ or short monitoring durations),

classical first-order kinetics remain adequate and the added parameter of HM-FOKM is not justified. A simple curvature ratio, $|H|/K^2$, is sometimes proposed as a rule-of-thumb screening criterion; however, this ratio should be applied with caution rather than as a strict decision rule. For example, Primary Control has a curvature ratio of 6.57 — well above any threshold that would nominally favour classical first-order — yet this treatment favours HM-FOKM on AICc (Table 9 note above), because its very small absolute H, though large relative to K^2, still improves the fit enough to offset the AICc parsimony penalty at n=8. The curvature ratio is therefore better understood as one contributing indicator among several (alongside monitoring duration and sample size) rather than a validated, universally reliable predictor of AICc outcome.

4. Discussion

4.1 A Structurally Simple Sensitivity Profile

The fixed-sign behaviour of S_K and S_H (Section 3.3) is a genuine structural simplification relative to models whose sensitivities change sign, where a single parameter can have opposite effects depending on monitoring time (Saltelli et al., 2008; Borgonovo and Plischke, 2016). This traces directly to the mechanistic derivation (Section 2.1): $K = k_0 - \alpha I_0$ is a catalytic-capacity parameter that can only increase degradation; $H = \alpha(p - v)$ is a net-hindrance parameter that can only suppress it. The model's behaviour is therefore not merely empirically adequate but mechanistically coherent.

For decelerating cases, both sensitivities diverge as t approaches t_{trans}, reflecting approach to the domain boundary rather than pathological biology. For accelerating cases, which possess no natural stall point, the sensitivities grow smoothly without diverging. This pattern suggests denser sampling near the end of the monitoring period for decelerating systems, and more evenly distributed sampling for accelerating ones.

4.2 The K–H Crossover: A Mechanistic Explanation for AICc Patterns

The $t \approx 9.8$-week crossover (Section 3.4) supplies the mechanistic complement to the validation study's empirical finding that AICc advantage tracks curvature strength. At short horizons the data contain too little information about H for it to matter, so a first-order fit loses almost nothing—consistent with the near-zero win rates in Dike (0 %) and Udume (33 %). Past the crossover, H's influence dominates the trajectory shape, consistent with the 100 % win rates in Ahmadi and Ritoré.

The crossover reflects the growing contribution of the quadratic $\frac{H}{2}t^2$ term relative to Kt as t increases, but it is a property of the pooled 48 000-point ensemble (Section 2.5), not of any individual treatment's own t_{trans}. Those values range from 7.9 to 33.5 weeks (Table 6) and should not be read as coinciding with the 9.8-week figure. The growing interaction/shared-variance term (Table 3) reflects the same K–H covariance documented in the profile-likelihood analysis (Section 3.6; mean $|\rho| = 0.924$); it also explains why $S_1(K)$ and $S_1(H)$ need not sum to 1 under correlated inputs.

4.3 Comparison with Classical First-Order Kinetics: Where the Added Complexity Earns Its Keep

Classical first-order kinetics has one parameter and the sensitivity function $S_k(t) = t\big(1 - B(t)\big)$, identical in form to HM-FOKM's $S_K(t)$. HM-FOKM's treatment of K is therefore a strict generalisation, not a departure (Rittmann and McCarty, 2001; Simkins and Alexander, 1984). The entire added statistical burden is attributable to H alone: it incurs a real identifiability penalty ($|\rho(K,H)|$ up to 0.982) and a variance contribution that is genuinely small at

short horizons, but it buys the ability to detect deceleration at all—a capability classical kinetics structurally cannot offer, because $h(t) = K$ is fixed by assumption (Alexander, 1999; Boopathy, 2000).

The K-to-H crossover (≈ 9.8 weeks) is, in effect, the minimum horizon at which this trade-off is likely to pay off statistically. Ritoré (100 % win rate; mean R^2 rising from 0.5581 to 0.8680; mean $\Delta\text{AICc} = -3.97$) exemplifies where the added complexity is valuable—strong curvature and a monitoring duration (20 weeks) long enough to observe it. Dike (0 % win rate; H only 0.0013–0.0017 week $^{-2}$; curvature ratio 0.54–0.74) exemplifies its limits: the data simply do not justify the extra parameter there.

4.4 The t_{90}/B_{proj} Correspondence and Implications for Experimental Design

The exact correspondence between the existence of t_{90} and $B_{\text{proj}} \geq 0.90$ (Section 3.8) means practitioners need not compute t_{90} separately: a single check of the already-available B_{proj} against 0.90 suffices. For accelerating systems, t_{90} supplies a direct benchmark comparable to the classical $\ln(10)/k$. For decelerating systems, its non-existence is itself a diagnostic result—a stronger, earlier warning than waiting for t_{trans}, because it signals from the fitted parameters alone that intervention (increased tilling, nutrient replenishment, aeration) is needed before the projected stall.

This t_{90}/B_{proj} check, together with the sensitivity and identifiability patterns above, motivates concrete monitoring-design guidance.

First, the K-to-H crossover (≈ 9.8 weeks; Section 4.2) implies that a programme targeting K alone can be short (1–4 weeks captures most of its variance), but resolving H reliably requires extending well past the crossover. This is consistent with H being well-constrained chiefly in the longer-duration, strong-curvature treatments identified in Section 3.6 (the Ahmadi pilots; Primary Control, CBC 8 900, NPK 8 900; Udume WH, SMC, SMC+WH). Concretely, monitoring intended to estimate H with confidence should extend to at least 12–16 weeks, with early sampling (weeks 1–5) weighted toward K and mid-phase sampling (weeks 6–12) toward H.

Second, once deceleration is detected, monitoring should extend to at least 1.3–$1.5\times$ the fitted t_{trans} (Section 3.7) in order to observe the stall directly and validate the projection. Ritoré's 20-week design, which captured one treatment's full deceleration trajectory, illustrates the value of this extension relative to the more conventional 8–12 weeks used elsewhere.

Third, the curvature ratio $|H|/K^2$ (Section 3.9) can serve as a rough additional screening indicator, though not as a substitute for computing AICc directly.

4.5 The Identifiability Trade-Off: A General Feature of Two-Parameter Saturating Models

The identifiability trade-off documented here—K well constrained, H much less so, the two strongly confounded—is not a peculiarity of HM-FOKM's particular functional form. The profile-likelihood results reveal a structural pattern consistent with other two-parameter saturating kinetic models: both exhibit strong negative correlations between their two parameters (HM-FOKM: $|\rho| = 0.890$–0.982, mean 0.924), and both show better constraint on the initial-rate parameter than on the curvature parameter in most treatments. This is not coincidental. Both are generalisations of a one-parameter exponential model obtained by adding a quadratic term to the exponent, and in both cases the resulting two-parameter model exhibits the same fundamental trade-off: the data can often be described equally well by different combinations of the two parameters, producing a negatively correlated parameter

space (Raue et al., 2009; Kreutz et al., 2012). The identifiability challenges documented here are therefore best read as a general property of two-parameter saturating kinetic models fitted to typical bioremediation time series, not an artefact of HM-FOKM's specific formulation (Bates and Watts, 1988; Ratkowsky, 1990).

The practical implication is that point estimates of H should be treated with caution, particularly when the 95 % confidence interval includes zero. In 10 of 24 treatments (41.7 %), H's confidence interval includes zero, meaning the classical first-order model ($H = 0$) cannot be statistically excluded even where HM-FOKM achieves a lower AICc. This does not mean HM-FOKM is unjustified in these cases—the AICc already accounts for the additional parameter (Burnham and Anderson, 2002)—but it does mean that practitioners should treat point estimates of H with caution and consider the $H = 0$ case as a plausible alternative interpretation of the same data. This is particularly important for regulatory applications, where the choice between first-order and hindrance-modified kinetics could affect remediation timelines and compliance decisions.

4.6 Limitations

Several limitations qualify the conclusions drawn here. First, the correlation-ratio ensemble, while grounded in the empirical (K, H) pairs from all 24 real treatments, is a specific choice; a differently-sourced validation set with different K or H values would shift the reported crossover time somewhat, though the qualitative K-to-H handoff should generalize (Saltelli et al., 2008; Borgonovo and Plischke, 2016). Second, the validation datasets remain limited to aerobic, mesophilic soil bioremediation contexts; extension to anaerobic, thermophilic, or aquatic systems has not been tested (Ossai et al., 2020; Ambaye et al., 2022). Third, the digitization uncertainty in datasets 3–5 cannot be entirely excluded, though endpoint validation supports calibration accuracy. Fourth, the strong K–H correlation (mean $|\rho| = 0.924$) raises the question of whether the two parameters are structurally identifiable at all with typical bioremediation monitoring schedules; the present analysis can only quantify that the correlation is high enough that point estimates of H should be treated with caution (Raue et al., 2009; Kreutz et al., 2012). Fifth, the mechanistic interpretation of K and H in terms of the tilling–volatilization mass balance (Section 2.1) is an interpretation, not a direct measurement; independent experimental validation (e.g., by measuring inhibitor concentrations or tilling efficacy) would be required to confirm the model's physical assumptions. Sixth, the t_{90} diagnostic's perfect correspondence with the H-sign split is a property of this particular validation dataset, not a general theorem—decelerating systems with sufficiently small H relative to K remain capable of a defined t_{90}, as the existence boundary in Figure 5 makes clear.

4.7 Future Directions

Several extensions follow naturally from this analysis. Extending the correlation-ratio framework to other two-parameter kinetic models would test whether the K-to-H crossover is a general feature of this model class or specific to HM-FOKM. Coupling the sensitivity framework with experimental design optimisation would provide precise guidance on optimal sampling schedules for resolving H in future bioremediation trials. Application of the t_{90} diagnostic to regulatory contexts, where 90% removal is a common benchmark (USEPA, 1996), would test its practical utility as a screening tool for remediation planning. Further validation of HM-FOKM on additional independent datasets—particularly with different contaminant types, soil conditions, and amendment strategies—would strengthen the evidence base for its generalisability. Extension of the profile-likelihood analysis to incorporate Bayesian priors from previous studies would allow formal quantification of how much additional information is needed to resolve H reliably (Kreutz et al., 2012; Raue et al., 2009). Finally, the mechanistic derivation suggests a specific experimental test: in a field trial with controlled tilling regimes, the sign and magnitude of H should

correlate with tilling frequency, with more frequent tilling producing more negative H and less frequent tilling producing more positive H.

4.5 Limitations

First, the correlation-ratio ensemble is grounded in this validation set's specific (K,H) values; a differently-sourced set would shift the reported crossover time somewhat, though the qualitative K-to-H handoff follows from the model's algebraic structure and should generalize (Saltelli et al., 2008; Borgonovo and Plischke, 2016). The ≈9.8-week figure is a characteristic time for this dataset, not a universal constant, and — as clarified in Section 4.2 — does not coincide with any individual treatment's own t_{trans}.

Second, the validation datasets, though diverse in geography and amendment strategy, remain limited to aerobic, mesophilic soil bioremediation; extension to anaerobic, thermophilic, or aquatic systems has not been tested and may require reassessment (Ossai et al., 2020; Ambaye et al., 2022) — anaerobic systems, for instance, may exhibit different hindrance mechanisms (e.g., volatile fatty acid or ammonia accumulation), and the tilling-driven volatilization mechanism motivating the zero-order removal assumption may not apply without mechanical aeration.

Third, digitization uncertainty in three datasets cannot be entirely excluded, though endpoint validation (0.0–2.4% agreement) and the Ritoré half-life check (0.4 days) support calibration accuracy; residual uncertainty of ±1–3 percentage points in B(t) could still affect parameter precision in small-sample or weak-curvature treatments.

Fourth, the strong K–H correlation (mean $|\rho|=0.924$), persisting even at the largest sample size (Primary, n=8) and mirrored in the DM-GKM's K–c collinearity, appears to be a fundamental property of two-parameter saturating kinetic models rather than a fitting artefact correctable by collecting more data of the same type; overcoming it would require independent information such as microbial biomass, enzyme activity, or inhibitor concentration measurements.

Fifth, the mechanistic interpretation of K and H via the tilling–volatilization mass balance (Section 2.1) is an interpretation, not a direct measurement — the lumped parameters aggregate intrinsic rate, initial inhibitor level, inhibition sensitivity, production rate, and removal rate, none separately identifiable from a biodegradability series alone. Independent validation (e.g., measuring inhibitor concentrations or tilling efficacy) is a priority for future work.

Sixth, the t_{90} diagnostic's perfect correspondence with the H-sign split is a property of this dataset's specific parameter combinations, not a general theorem: the existence boundary $H=K^2/(2\cdot\ln 10)$ in Figure 5 shows that decelerating systems with sufficiently mild hindrance remain capable of reaching 90% removal. Practitioners should compute B_{proj} directly rather than assume deceleration implies automatic failure to reach the benchmark.

4.6 Future Directions

Extending the correlation-ratio framework to other two-parameter kinetic models would test whether the K-to-H crossover generalizes beyond HM-FOKM. Coupling the sensitivity framework with experimental design optimisation could identify the most informative sampling time points directly (Bates and Watts, 1988; Raue et al., 2009), and applying the t_{90} diagnostic to regulatory contexts (USEPA, 1996) would test its practical utility for remediation planning. Further validation on independent datasets with different contaminants, soils, and amendments would strengthen generalisability claims; incorporating Bayesian priors into the profile-likelihood analysis (Kreutz et al., 2012; Raue et al., 2009) would help quantify how much additional information is needed to resolve H reliably; and a user-friendly software implementation automating all diagnostics (t_{trans}, B_{proj}, t_{90}) would facilitate practitioner adoption.

The mechanistic derivation from the tilling–volatilization mass balance suggests a direct experimental test: in a field trial with controlled tilling regimes, H's sign and magnitude should correlate with tilling frequency — more frequent

tilling producing more negative H, less frequent tilling more positive H. Such an experiment would provide direct validation of the model's physical assumptions.

Declarations

Acknowledgements

The author acknowledges the support provided by the University of Port Harcourt for the field experimental site and laboratory facilities. The contributions of technical staff in the Department of Microbiology and the Environmental Research Laboratory are gratefully acknowledged.

Funding

No funding was received for conducting this study.

Authors' Contributions

Momoh, O.L.Y. conceived and designed the study, developed the kinetic model, performed all statistical analyses (local sensitivity, global sensitivity via correlation-ratio and Sobol methods, profile-likelihood identifiability analysis), curated and validated the data, created all visualizations, and wrote and revised the manuscript.

Ethical Approval

Not applicable. This study did not involve human participants, human data, or human tissue, nor did it involve animal experiments.

Consent to Participate

Not applicable. This study did not involve human participants.

Consent to Publish

Not applicable. This study does not contain data from any individual person.

Competing Interests

The author declares no competing financial or non-financial interests. The author has no relevant financial or non-financial interests to disclose.

Data Availability Statement

The datasets generated and/or analysed during the current study are available from the corresponding author on reasonable request. All data used in this study are either published with open access and cited within the manuscript (with DOIs provided)

References

Ahmadi M, Dashtestani M, Takdastan A, Jorfi S, Ramavandi B (2016) Data on biodegradation of total petroleum hydrocarbons using co-composting of cow manure/oily drill wastes. Data Brief 9:723–726. https://doi.org/10.1016/j.dib.2016.10.008

Alexander M (1999) Biodegradation and Bioremediation, 2nd edn. Academic Press, San Diego

Ambaye TG, Chebbi A, Formicola F, Rosatelli A, Prasad S, Gomez FH, Sbaffoni S, Franzetti A, Vaccari M (2022) Ex-situ bioremediation of petroleum hydrocarbon contaminated soil using mixed stimulants: response and dynamics of bacterial community and phytotoxicity. J Environ Chem Eng 10(6):108814. https://doi.org/10.1016/j.jece.2022.108814

Atlas RM, Hazen TC (2011) Oil biodegradation and bioremediation: a tale of the two worst spills in U.S. history. Environ Sci Technol 45(16):6709–6715. https://doi.org/10.1021/es2013227

Bates DM, Watts DG (1988) Nonlinear Regression Analysis and Its Applications. Wiley, New York. https://doi.org/10.1002/9780470316757

Bekins BA, Warren E, Godsy EM (1998) A comparison of zero-order, first-order, and Monod biotransformation models. Ground Water 36(2):261–268. https://doi.org/10.1111/j.1745-6584.1998.tb01091.x

Boopathy R (2000) Factors limiting bioremediation technologies. Bioresour Technol 74(1):63–67. https://doi.org/10.1016/S0960-8524(99)00144-3

Borgonovo E, Plischke E (2016) Sensitivity analysis: a review of recent advances. Eur J Oper Res 248(3):869–887. https://doi.org/10.1016/j.ejor.2015.06.032

Burnham KP, Anderson DR (2002) Model Selection and Multimodel Inference: A Practical Information-Theoretic Approach, 2nd edn. Springer, New York. https://doi.org/10.1007/b97636

Chen T, Zhang Y, Dong Y (2024) Bioremediation experiments and dynamic model of petroleum hydrocarbon contaminated soil. J Environ Manage 365:121247. https://doi.org/10.1016/j.jenvman.2024.121247

Dike CC, Krohn C, Khudur LS, Batra AR, Nnorom MA, Surapaneni A, Shah K, Ball AS (2024) Impact of biosolids-derived biochar on the remediation and ecotoxicity of diesel-impacted soil. Soil Syst 8(2):40. https://doi.org/10.3390/soilsystems8020040

Grau P, Dohanyos M, Chudoba J (1975) Kinetics of multicomponent substrate removal by activated sludge. Water Res 9(7):637–642. https://doi.org/10.1016/0043-1354(75)90169-4

Hamby DM (1994) A review of techniques for parameter sensitivity analysis of environmental models. Environ Monit Assess 32(2):135–154. https://doi.org/10.1007/BF00547132

Herman J, Usher W (2017) SALib: an open-source Python library for sensitivity analysis. J Open Source Softw 2(9):97. https://doi.org/10.21105/joss.00097

Jakubauskaitė V, Žukauskaitė A, Gasiūnas S, Kliucininkas L (2024) Model-centric optimisation of biochemical remediation of petroleum hydrocarbon contaminated soil. Soil Use Manag 40:e12983. https://doi.org/10.1111/sum.12983

Jiao S, Chen W, Wei G (2016) Microbial succession in response to pollutants in the environment: a review. J Environ Sci 42:10–20. https://doi.org/10.1016/j.jes.2015.09.012

Kreutz C, Raue A, Timmer J (2012) Likelihood-based observability analysis and confidence intervals for predictions of dynamic models. BMC Syst Biol 6:120. https://doi.org/10.1186/1752-0509-6-120

Leahy JG, Colwell RR (1990) Microbial degradation of hydrocarbons in the environment. Microbiol Rev 54(3):305–315. https://doi.org/10.1128/mr.54.3.305-315.1990

Marquardt DW (1963) An algorithm for least-squares estimation of nonlinear parameters. J Soc Ind Appl Math 11(2):431–441. https://doi.org/10.1137/0111030

Megharaj M, Ramakrishnan B, Venkateswarlu K, Sethunathan N, Naidu R (2011) Bioremediation approaches for organic pollutants: a critical perspective. Environ Int 37(8):1362–1375. https://doi.org/10.1016/j.envint.2011.06.003

Momoh Y (2025) Modifying the Baranyi–Roberts model for studying bioremediation kinetics in crude-oil contaminated soil. Discover Soil 2:52. https://doi.org/10.1007/s44378-025-00071-2

Motulsky HJ, Ransnas LA (1987) Fitting curves to data using nonlinear regression: a practical and nonmathematical review. FASEB J 1(5):365–374. https://doi.org/10.1096/fasebj.1.5.3315805

Nweke CN, Nwabanne JT (2021) Anaerobic digestion of yam peel for biogas production: a kinetic study. J Eng Appl Sci 18(1):275–286

Ossai IC, Ahmed A, Hassan A, Hamid FS (2020) Remediation of soil and water contaminated with petroleum hydrocarbon: a review. Environ Technol Innov 17:100526. https://doi.org/10.1016/j.eti.2019.100526

Ratkowsky DA (1990) Handbook of Nonlinear Regression Models. Marcel Dekker, New York

Raue A, Kreutz C, Maiwald T, Bachmann J, Schilling M, Klingmüller U, Timmer J (2009) Structural and practical identifiability analysis of partially observed dynamical models by exploiting the profile likelihood. Bioinformatics 25(15):1923–1929. https://doi.org/10.1093/bioinformatics/btp358

Ritoré E, Arnaiz C, Morillo J, Egea-Corbacho A, Usero J (2025) Use of liquid industrial by-products as biostimulants in the remediation of hydrocarbon-contaminated soils. Clean Technol 7(4):114. https://doi.org/10.3390/cleantechnol7040114

Rittmann BE, McCarty PL (2001) Environmental Biotechnology: Principles and Applications. McGraw-Hill, New York

Saltelli A, Annoni P, Azzini I, Campolongo F, Ratto M, Tarantola S (2010) Variance based sensitivity analysis of model output: design and estimator for the total sensitivity index. Comput Phys Commun 181(2):259–270. https://doi.org/10.1016/j.cpc.2009.09.018

Saltelli A, Ratto M, Andres T, Campolongo F, Cariboni J, Gatelli D, Saisana M, Tarantola S (2008) Global Sensitivity Analysis: The Primer. Wiley, Chichester. https://doi.org/10.1002/9780470725184

Schimel JP, Schaeffer SM (2012) Microbial control over carbon cycling in soil. Front Microbiol 3:348. https://doi.org/10.3389/fmicb.2012.00348

Simkins S, Alexander M (1984) Models for mineralization kinetics with the variables of substrate concentration and population density. Appl Environ Microbiol 47(6):1299–1306. https://doi.org/10.1128/AEM.47.6.1299-1306.1984

Sobol IM (2001) Global sensitivity indices for nonlinear mathematical models and their Monte Carlo estimates. Math Comput Simul 55(1–3):271–280. https://doi.org/10.1016/S0378-4754(00)00270-6

Storn R, Price K (1997) Differential evolution—a simple and efficient heuristic for global optimization over continuous spaces. J Glob Optim 11(4):341–359. https://doi.org/10.1023/A:1008202821328

Udume OA, Abu GO, Stanley HO, Vincent-Akpu IF, Momoh Y, Eze MO (2023) Biostimulation of petroleum-contaminated soil using organic and inorganic amendments. Plants 12(3):431. https://doi.org/10.3390/plants12030431

USEPA (1996) Method 8061A: Phthalate Esters by Gas Chromatography with Electron Capture Detection (GC/ECD), Revision 1. U.S. Environmental Protection Agency, Washington, DC

Varjani SJ (2017) Microbial degradation of petroleum hydrocarbons. Bioresour Technol 223:277–286. https://doi.org/10.1016/j.biortech.2016.10.037

Venzon DJ, Moolgavkar SH (1988) A method for computing profile-likelihood-based confidence intervals. J R Stat Soc Ser C Appl Stat 37(1):87–94. https://doi.org/10.2307/2347496

Zwietering MH, Jongenburger I, Rombouts FM, Van't Riet K (1990) Modeling of the bacterial growth curve. Appl Environ Microbiol 56(6):1875–1881. https://doi.org/10.1128/AEM.56.6.1875-1881.1990